Table of Contents

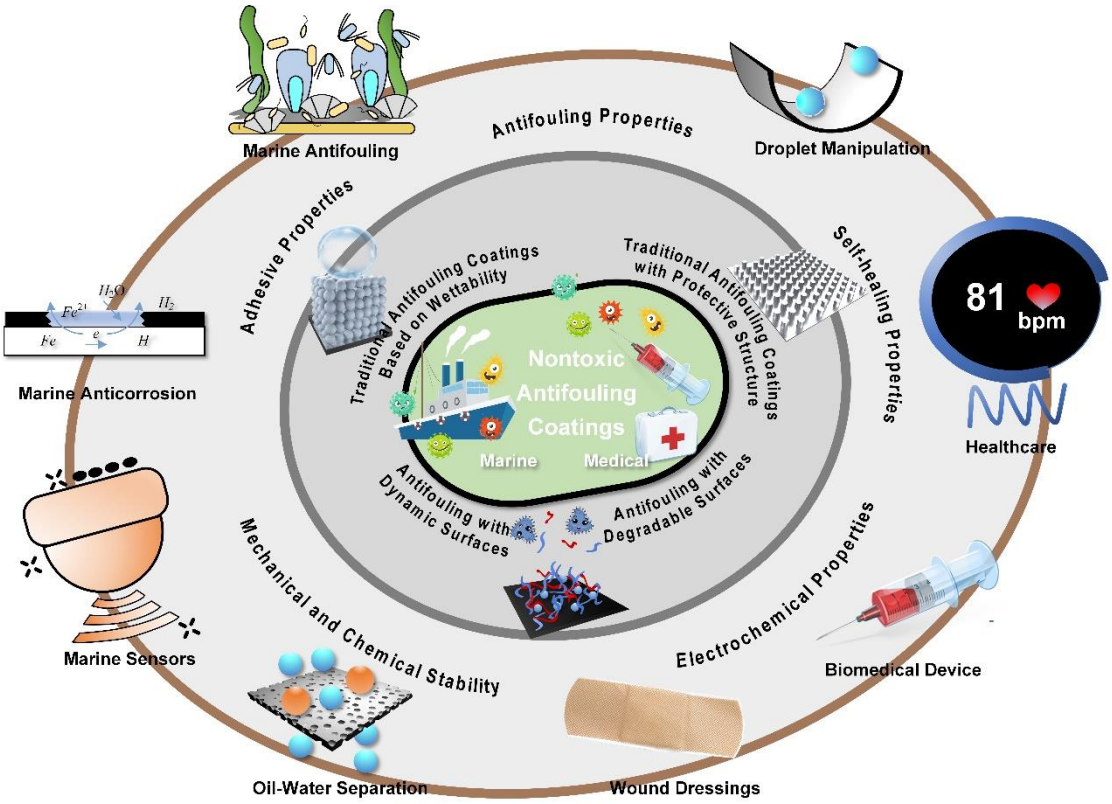

Non-Toxic Evolution: Advances in Multifunctional Antifouling Coatings

Xuerui Zang[a, b], *Yimeng Ni*[c], *Qiuyan Wang*[a, b], *Yan Cheng*[c, f, g], *Jianying Huang*[c, f], *Xuewen Cao*[b, *], *Claire J. Carmalt*[h, *], *Yuekun Lai*[c, f, *], *Dong Ha Kim,*[d, *] *Yijiang Liu,*[e, *] and *Zhiqun Lin*[a,d *]

[a] Department of Chemical and Biomolecular Engineering, National University of Singapore, Singapore 117585, Singapore

[b] College of Pipeline and Civil Engineering, China University of Petroleum (East China), Qingdao 266580, P. R. China

[c] College of Chemical Engineering, Fuzhou University, Fuzhou 350116, P. R. China

[d] Department of Chemistry and Nano Science, Ewha Womans University, 52 Ewhayeodae-gil, Seodaemun-gu, Seoul 03760, Republic of Korea

[e] College of Chemistry, Key Lab of Environment-Friendly Chemistry and Application in Ministry of Education, Xiangtan University, Xiangtan 411105, Hunan Province, P. R. China.

[f] Qingyuan Innovation Laboratory, Quanzhou 362801, P. R. China

[g] Zhejiang Engineering Research Center for Tissue Repair Materials, Joint Centre of Translational Medicine, Wenzhou Institute, University of Chinese Academy of Science, Wenzhou, Zhejiang 325000, P. R. China

[h] Department of Chemistry, University College London, 20 Gordon Street, London WC1H 0AJ, U.K.

E-mail: caoxw@upc.edu.cn (X. Cao); c.j.carmalt@ucl.ac.uk (C. J. Carmalt) yklai@fzu.edu.cn (Y. Lai); dhkim@ewha.ac.kr (D. H. Kim); liuyijiang84@xtu.edu.cn (Y. Liu); and z.lin@nus.edu.sg (Z. Lin)

Abstract

Antifouling coatings play a crucial role in preventing the adhesion of marine organisms, bacteria, and blood, making them a primary strategy for combating biofouling in the marine industry. However, conventional antifouling coatings suffer from drawbacks such as high toxicity, limited abrasion resistance, and unstable polymer degradation rates, which can have

adverse effects on the environment, economy, and human health. Thus, there is an urgent need for the development of sustainable and nontoxic antifouling coatings. This review first presents four major antifouling strategies: traditional coatings based on wettability, traditional coatings with protective structures, nontoxic coatings based on main chain degradable polymers, and nontoxic coatings combining main chain degradation with branch chain hydrolysis polymers. Second, the review provides a comprehensive overview of antifouling coatings with diverse functionalities, including antibacterial, anti-protein, anti-blood, anti-incrusting, adhesive, self-healing, and corrosion-resistant properties. Then, the application of antifouling coatings in marine environments and the medical field is thoroughly explored. Additionally, the review addresses the current challenges encountered by antifouling coatings. Finally, a forward-looking perspective is presented, envisioning future advancements in this field. By addressing these aspects, this review aims to stimulate further development and innovation in the realm of antifouling coatings.

Keywords: Antifouling coatings; Marine biofouling; medical biofouling; non-toxic antifouling; Multifunctional antifouling coatings

1. Introduction

Adhesion is a pervasive phenomenon with wide-ranging implications in everyday life, yielding consequential effects that can result in unforeseen economic losses and safety hazards across diverse industries [1]. Extended submersion of ships in the ocean leads to substantial colonization on their surfaces, as marine fouling organisms such as plants, animals, and microorganisms proliferate **(Figures 1A, 1B)**. The presence of these organisms not only increases resistance during ship navigation, resulting in elevated fuel consumption and decreased maneuverability, but also introduces issues such as sonar interference [2]. According to estimates by the US Navy Command, the buildup of biological deposits on a ship's hull can lead to a speed loss of approximately 2% and fuel cost increases ranging from 6% to 45%, contingent upon vessel size [3]. Furthermore, in the domain of oil and gas transportation

pipelines, the adhesion of impurities, exemplified in **Figure 1C**, exerts a pronounced negative impact on material transfer efficiency [4]. This phenomenon can give rise to flow channel obstructions and heightened fluid resistance. Therefore, it often mandates the temporary cessation of pipeline operations for mechanical cleaning, resulting in a decline in operational efficiency and substantial economic repercussions. In addition, biofouling poses a significant challenge in the biopharmaceutical industry **(Figure D)**, particularly when it comes to the adhesion of bacteria or histiocytes to medical devices [5]. This undesired adhesion has detrimental effects on multiple fronts. Firstly, the contamination of medical devices by bacteria increases the risk of infections. Secondly, when histiocytes adhere to medical devices implanted in the body, such as bioengineered scaffolds, it results in the loss of their functionality. The cardiovascular implantable electronic devices (CIEDs)-related infection is a serious complication [6]. According to the medical linkage system of the Rochester Epidemiology Project, almost 1 in 4 patients who undergo ⩾2 CIEDs replacements develops infection [7].

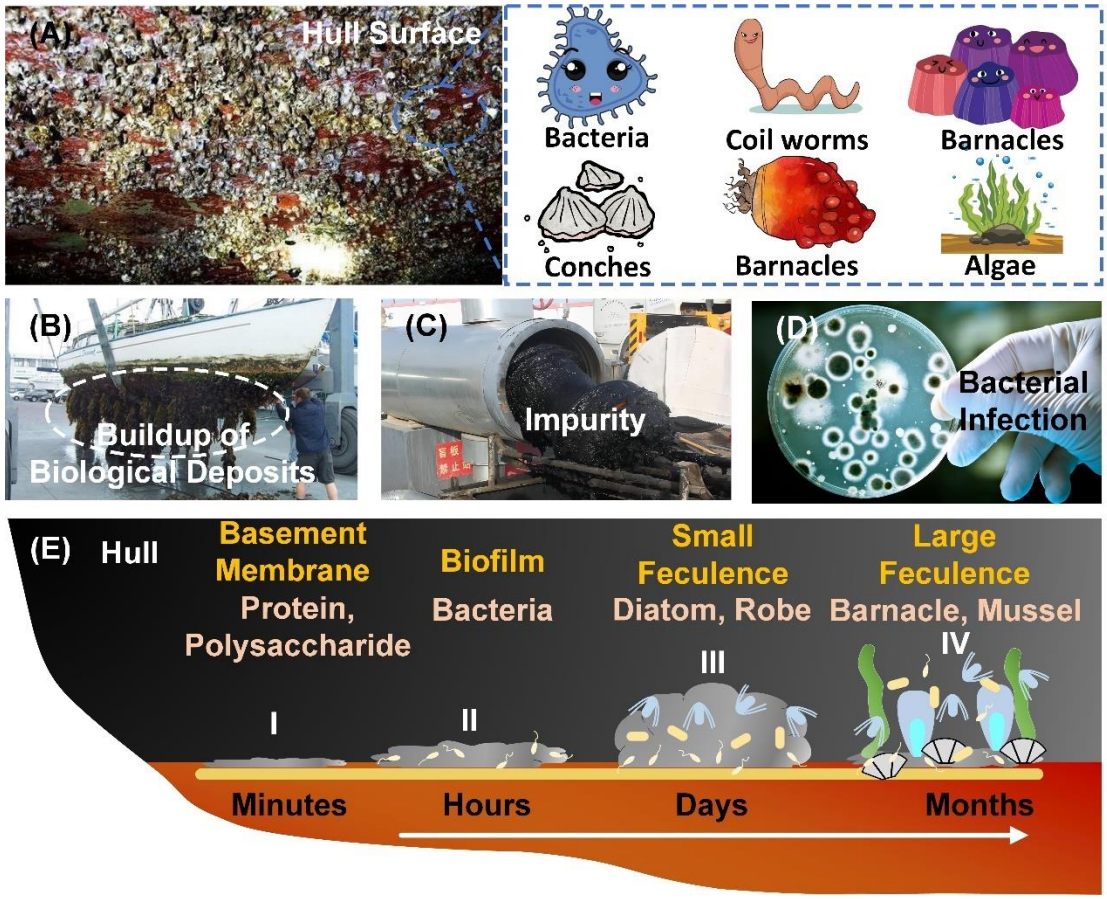

Figure 1 (A) Biological adhesion on the surface of the ship, including bacteria, coil worms, barnacles, conches, algae, etc. **(B)** Bioaccumulation on the hull surface. **(C)** Impurities adhering

to the inner wall of the pipeline. **(D)** Surfaces of medical equipment harboring adherent microbial communities. **(E)** The process of biological attachment to the surface of equipment. In the realm of medicine, it encompasses exclusively two processes: Processes I and II.

Biological fouling is a dynamic process characterized by temporal and spatial variations [8]. Our study endeavors to devise methodologies for the prevention and control of biological fouling by scrutinizing the attributes of the marine environment and the intricacies of the fouling process **(Figure 1E)**. In light of fouling characteristics, we can delineate the adsorption process of the organisms into four distinct stages. Initially, during the first stage, organic and inorganic macromolecules such as proteins and polysaccharides rapidly adsorb onto the surfaces of underwater structures, forming a foundational film. Subsequently, in the second stage, marine bacteria and other microorganisms adhere to and proliferate on the substrate, forming a biofilm that firmly attaches to the facility's surface by secreting extracellular polymers. Moving to the third stage, within a few days, small multicellular fouling organisms, such as diatoms, further colonize and reproduce upon the existing biofilm, resulting in the formation of a slimy layer. Finally, in the fourth stage, which occurs over a span of one to two months, numerous large fouling organisms, including barnacles, mussels, large algae, and coil worms, progressively attach, grow, and extensively cover the facility's surface over an extended period. Hence, proteins and bacteria serve as primary instigators of biological adhesion to substrate surfaces [9]. The development of antibacterial, anti-protein coatings and the implementation of corresponding preventive measures represent efficacious approaches to combat biological adhesion [10]. Through the resolution of these challenges, we can envisage a reduction in resistance, optimization of material transfer efficiency, and mitigation of the economic and operational impacts arising from adhesion in diverse industrial sectors.

In this review, we present an overview of the recent advancements in the development of multifunctional non-toxic antifouling coatings for marine and medical applications. The review is structured as follows: Firstly, we provide a comprehensive summary of representative antifouling coatings. These include traditional antifouling coatings that rely on surface wettability, antifouling coatings incorporating protective structures, non-toxic antifouling coatings based on main chain degradable polymers, and non-toxic antifouling coatings utilizing

main chain degradation and branch chain hydrolysis polymers. Secondly, we delve into the diverse range of functionalities exhibited by antifouling coatings. Specifically, we discuss their effectiveness against biological fouling, bacterial fouling, blood fouling, scale fouling, as well as their self-healing properties, antifreeze capabilities, corrosion resistance, adhesion properties, and mechanical stability. Thirdly, we explore the notable applications of antifouling coatings in both the marine industry and medical fields. These applications encompass marine antifouling and drag reduction, marine corrosion prevention, oil-water separation, marine sensor technologies, wound dressings, and biomedical and healthcare equipment. Finally, we address the future challenges and prospects associated with non-toxic antifouling coatings, highlighting areas that require further research and development. By presenting this comprehensive review, we aim to contribute to the understanding of the latest advancements in multifunctional non-toxic antifouling coatings, while shedding light on their potential applications in marine and medical domains.

2. Classifications of antifouling coatings

2.1 Traditional antifouling coatings based on wettability

Traditional antifouling coatings predominantly include fouling release coatings (FRC) [11] [12] [13], self-polishing coatings (SPC) [14] [15] [16] and zwitterionic antifouling coatings [17] [18] [19], etc., all relying on surface characteristics that enhance wettability [20]. FRC coatings possess a smooth surface, low surface energy, and high elasticity, making it difficult for fouling organisms to adhere or firmly attach. SPC coatings, on the other hand, are composed of a vinyl polymer with hydrolyzable side groups like silyl, copper, and zinc ester, which can react with seawater in a controlled manner. The antifouling mechanism of zwitterionic coatings is indeed primarily attributed to the formation of a dense hydration layer on the surface through their hydrophilic properties. This hydration layer effectively repels foulants by presenting a highly hydrated and charged interface, thereby effectively preventing the fouling adhesion of marine organisms and other contaminants.

Several studies have provided compelling evidence supporting the role of hydration layers

in the antifouling properties of zwitterionic coatings. For example, Molino et al. [21] conducted a comprehensive investigation into the fouling resistance of zwitterionic polymer brushes and found a significant reduction in protein adsorption due to the hydration layer formed on the polymer surface. Similarly, Wellens et al. [22] explored the fouling behavior of zwitterionic surfaces using quartz crystal microbalance with dissipation monitoring (QCM-D) and atomic force microscopy (AFM), demonstrating that the hydration layer effectively repelled foulants and inhibited their adhesion. Furthermore, theoretical studies have provided insights into the molecular mechanisms underlying the formation and stability of hydration layers on zwitterionic surfaces. Molecular dynamics simulations by Deng et al. [23] revealed that the hydration layer is stabilized by strong electrostatic interactions between water molecules and charged functional groups within the zwitterionic structure, resulting in a robust and dynamic barrier against foulant attachment. Moreover, in vivo studies have demonstrated the practical efficacy of zwitterionic coatings in real-world marine environments. For instance, Zhang et al. [24] evaluated the fouling resistance of zwitterionic coatings on marine vessels through long-term field trials and observed significantly reduced fouling compared to conventional coatings, highlighting the effectiveness of hydration layers in preventing biofouling.

Furthermore, the traditional antifouling efficacy of these coatings depends on interfacial shear forces and often exhibits reduced effectiveness in stagnant water environments. To bolster their anti-adhesion performance, the incorporation of toxic reagents, such as antimicrobial and antifouling agents [25], is employed to actively eliminate adherent organisms from the surface.

Lubricin (LUB) [26] with unique "bottle brush" molecular structure is an excellent antifouling agent in the medical field with high viscosity resistance and extremely low friction coefficient. Xia et al. [26] conducted a study in which bottlebrush polymers were synthesized using a straightforward drop-casting or online exposure technique **(Figure 2A)**. The introduction of adhesive blocks from LUB into the polymer structure significantly improved the stability of the resultant coating. The superior antifouling properties of the coating were confirmed through experiments involving three distinct proteins and a bacterium **(Figure 2B)**.

The exceptional antifouling performance of the coating primarily stems from the substantial steric hindrance and hydration repulsion provided by the polymer surface of the bottlebrush. These bottlebrush polymers demonstrated the ability to effectively prevent long-term adhesion of various proteins and bacteria. Intriguingly, surface force microscopy (SFA) analysis revealed that even under high-pressure conditions, the polymer monolayers maintained their antifouling properties.

In the marine field, a self-polishing antifouling coating strategy based on phenol ester hydrolysis has been introduced. This approach utilizes a one-step method to incorporate a quaternary ammonium salt into a eugenol ester-based methacrylate resin, resulting in the formation of EMQFP [27] (poly (eugenol methacrylate acryloxyethyl trimethylammonium chloride hexafluorobutyl methacrylate methyl methacrylate butyl methacrylate ethylene glycol methyl ether acrylate)) **(Figure 2C)**. The inclusion of quaternary ammonium cations in the coating enables interaction with the π structure of the eugenol benzene ring, anchoring eugenol onto the coating surface and forming a novel zwitterionic-like structure through conformational adjustments. Subsequent hydrolysis increases the eugenol concentration on the coating surface, significantly enhancing its antifouling performance **(Figure 2D)**. This developed coating exhibits remarkable inhibitory effects against bacterial, diatom, and mussel adhesion, thereby establishing its efficacy as an antifouling agent **(Figure 2E)**. Silicone oil [28-30] is another commonly used antifouling agent with low surface tension, which eliminates the need for side chain hydrolysis like SPC to achieve antifouling performance. In a comprehensive investigation, Miserez et al. [1] explored the mechanism of mussel adhesion on surfaces, incorporating principles from thermodynamics and fracture mechanics. By incorporating silicone oil as a lubricant into polydimethylsiloxane (PDMS), they created a modified coating known as i-PDMS, which effectively prevents mussel adhesion **(Figure 2F)**. The authors utilized theoretical calculations to elucidate the underlying principles governing the exceptional antifouling performance of i-PDMS. The total adhesion energy G_c is the sum of the thermodynamic work of adhesion W_a at the interface (molecular interfacial energy due to the adhesive proteins) and of the viscoelastic dissipative process due to plaque and thread

deformation (W_e). For the non-infused surface, the liquid is water, whereas for the infused surfaces, the liquid is the infused lubricant. The vanguard Pvfp-5 adhesive protein efficiently displaces molecular-bound water on non-infused surfaces, whereas residual lubricant may remain at the interface for the infused surfaces, owing to the ultralow interfacial energy between the substrate and the lubricant, leading to partial plaque/substrate contact. Their findings underscore the critical role of the exceptionally low interfacial energy of i-PDMS in repelling fouling organisms, consistent with experimental demonstrations of its outstanding macroscopic antifouling properties **(Figures 2G, 2H)**.

Surface wettability assumes a paramount role in the development of traditional antifouling coatings, serving as a critical factor for achieving fouling release and enhancing antifouling performance. It is governed by both surface energy and morphology. Surface energy, in particular, plays a pivotal role in the formation of scale on solid surfaces. Low surface energy FRC coating effectively mitigate the interaction between organisms and substrates, resulting in minimal bio-adhesion. Additionally, surface morphology directly influences the contact area for fouling adhesion, with a smaller contact area necessitating less force for fouling removal. Notably, antifouling coatings incorporating zwitterions exhibit unique antifouling mechanisms. Their hydrophilic properties give rise to a dense hydration layer on the surface, showcasing exceptional antifouling capabilities. In light of these advantages, the successful development of antifouling coatings based on (super)hydrophobic, (super)hydrophilic, and amphiphilic surface wettability paves the way for the design of non-toxic and durable coatings across diverse domains, including marine, industrial, and medical applications.

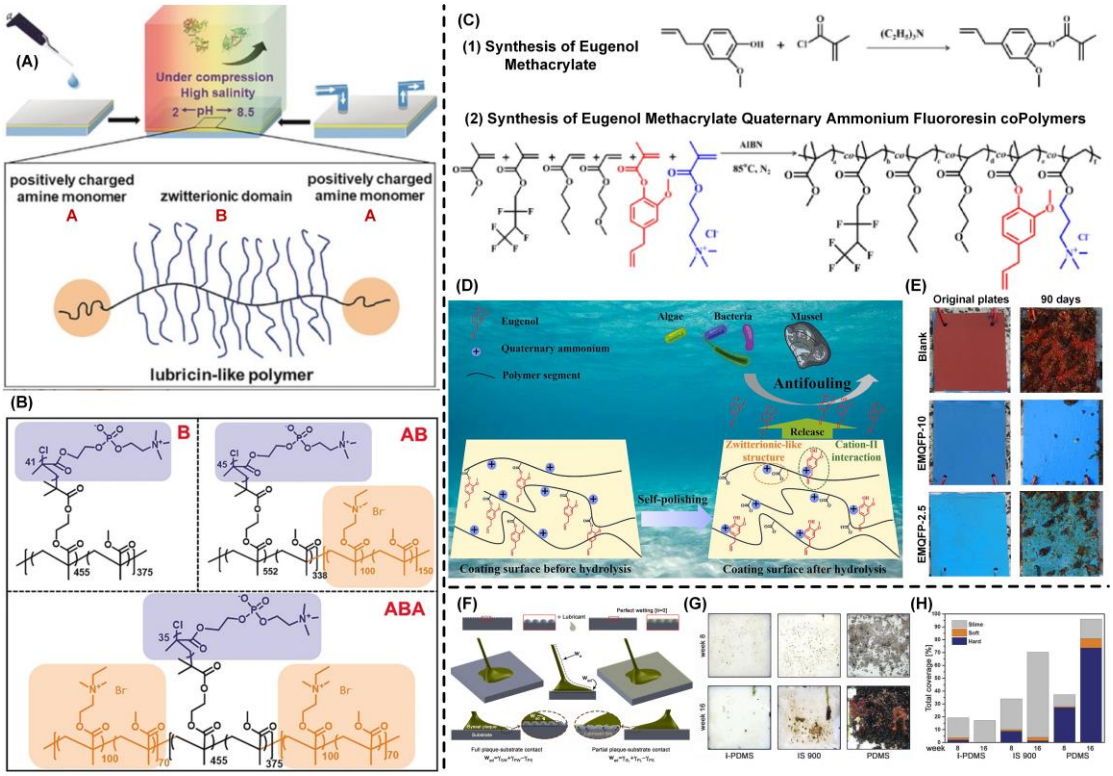

Figure 2 (A) Schematic diagram of the antifouling surface synthesis mechanism of lubricin-like microstructure LUB@PMPC coatings. **(B)** The molecular structures of ABA, AB, and B polymers. The anchoring side groups are depicted in orange and the pendant zwitterionic chains of the bottlebrush polymers are in blue. **(C)** The synthesis of the EM and EMQFPs via free radical polymerization. **(D)** Schematic diagram of the antifouling mechanism of a SPC coating based on eugenol and phenolic ester groups. **(E)** Photographs of the EMQFP coatings and blank immersed in the Yellow Sea of China for 90 days. **(F)** Adhesion mechanics of mussel threads on non-infused (left) and infused (right) surfaces. **(G)** Representative images for the fouling communities associated with each surface type after 8 and 16 weeks of static immersion on 175 mm by 175 mm substrates. **(H)** Total coverage and composition of the fouling communities.

2.2 Antifouling coating with protective structure

Microstructural antifouling coatings are characterized by incorporating diverse-shaped microstructures, such as convex columns [31-33], pits [13, 34, 35], and groove-shaped [36-38] regular structures, on the coating surface **(Figure 3A)**. These coatings exhibit significant improvements in mechanical properties compared to traditional antifouling coatings. The microstructures serve a dual purpose: protecting surface micro and nano particles against loss caused by external forces and contributing to the superhydrophobic properties of the coating. The regular micro texture, combined with the low surface energy of the coating, reduces the adhesion area and strength between the surface and microorganisms, thus achieving long-term

antifouling objectives [39].

Deng et al. [40] successfully developed a superhydrophobic ceramic coating with an armor microstructure, capitalizing on the ceramic's low surface energy and high hardness **(Figure 3B)**. Photolithography techniques were employed on silicon substrates to fabricate inverted pyramid microstructures with an approximate angle of α=125° **(Figure 3C)**. The coating exhibited remarkable durability, maintaining static and dynamic water contact angles above 150° and below 10°, respectively, even after undergoing 1000 sandpaper wear tests **(Figure 3D)**. Finite element method simulations and micro-indentation testing confirmed the exceptional mechanical stability of the surface textures, withstanding a maximum applied load of 45 N with minimal damage. Achieving robust superhydrophobicity in this coating relied on the construction of microstructures at two distinct length scales. The nanostructure design ensured waterproofing, while the micron skeleton structure design provided durability. The microstructure consisted of an interconnected surface frame enclosing water-responsive and mechanically fragile nanostructures within "pockets". This surface frame acted as protective "armor", safeguarding the nanostructures against removal by abradants larger than the frame size.

Polyvinylidene fluoride (PVDF) [41] is another widely used micro-structured superhydrophobic film layer known for its exceptional mechanical properties, bacterial resistance, and aging resistance. It finds extensive applications in areas such as seawater pollution prevention, filtration, and battery separators. Successful fabrication of micro-structured thin films with cylindrical hole arrays has been achieved using the silicon template method. Micro-forming involves employing a silicon template on a PDMS substrate **(Figures 3E, 3F)**. Permeation experiments utilizing a supersaturated $CaSO_4$ solution of 2000 $mg \cdot L^{-1}$ demonstrate that the cumulative permeation volume function ($J \cdot J_0^{-1}$) approaches unity, indicating minimal scaling phenomena on the surface of the CF_4-MP-PVDF film. Furthermore, the introduction of CF_4-modified MP-PVDF film yields a porous hydrophobic film with high contact angle and low surface porosity. According to classical nucleation theory, the Gibbs free energy required for surface fouling formation in the CF_4-MP-PVDF film is calculated to be 33

mJ·mol^{-1}, suggesting a higher energy barrier for heterogeneous nucleation **(Figure 3G)**. Consequently, the film exhibits excellent antifouling performance due to the challenging conditions required for surface fouling, leading to limited fouling occurrence.

The successful development of microstructure-based antifouling coatings represents an innovative approach for crafting environmentally friendly coatings possessing enduring, stable, and efficient self-cleaning, antifouling, or heat transfer properties, especially in demanding operational settings. This advancement unlocks opportunities for formulating advanced coatings capable of enduring harsh conditions while delivering the desired functionalities. Nevertheless, as previously noted, the removal of fouling organisms relies on the application of shear forces, demanding a specific speed to effectively counter contamination. Consequently, the antifouling effectiveness of these coatings remains somewhat restricted for temporarily stationary vessels or other marine structures with limited mobility.

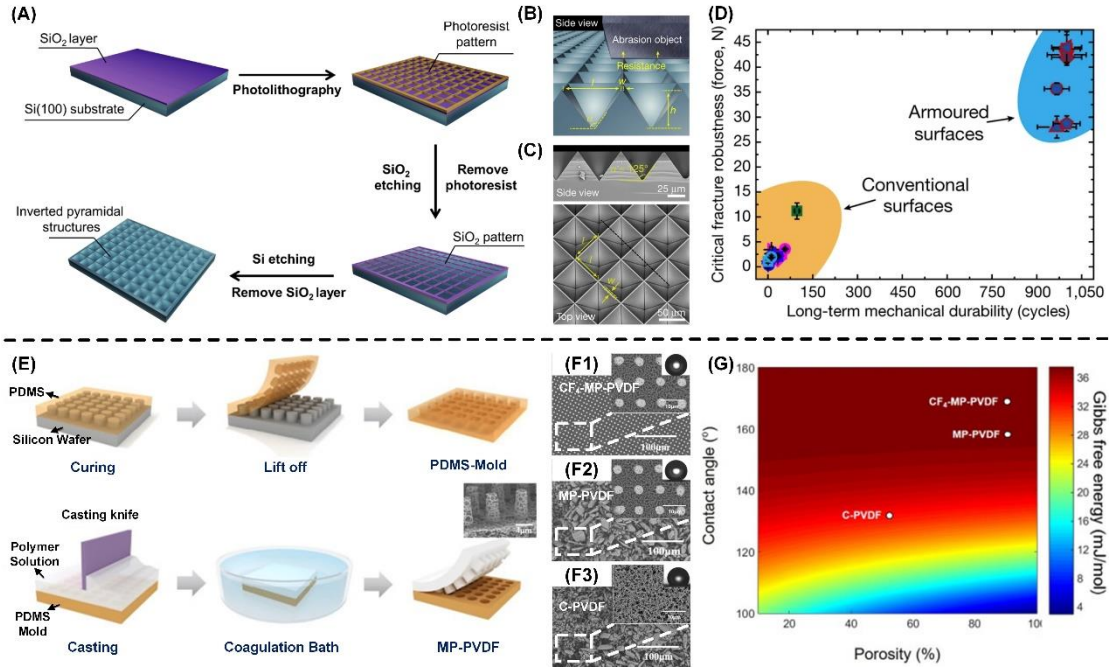

Figure 3 (A) The scheme of fabrication of the inverted-pyramidal substrates. **(B)** The microstructure framework consists of an array of microscale inverted-pyramidal cavities. **(C)** SEM of the inverted-pyramidal structures on silicon substrates. **(D)** Comparison of the mechanical stabilities of different superhydrophobic surfaces. **(E)** Schematic for the fabrication of micro-pillar PVDF (MP-PVDF) membrane. **(F)** SEM images of CF_4-MP-PVDF (F1), MP-PVDF (F2) and C-PVDF (F3) membrane top surface and the corresponding water wetting state of the membranes (SCA: 167° (CF_4-MP-PVDF); 155.3° (MP-PVDF); 130.1° (C-PVDF)). **(G)** Map of Gibbs free energy for the formation of $CaSO_4$ crystal as a function of contact angle

(ranges from 100 to 180°) and surface porosity.

The descriptions in sections 2.1 and 2.2 delineate how traditional antifouling coatings utilize surface wettability to prevent fouling, with FRC, SPC, zwitterionic, and structurally fortified coatings each presenting distinct advantages. However, wettability-based antifouling coatings, particularly zwitterionic coatings as exemplars of flexible coatings, often exhibit inadequate mechanical properties, resulting in a brief antibacterial efficacy period. Moreover, as discussed earlier, the antibacterial effect of wettable surface coatings in stagnant water environments is constrained in the absence of fungicides, necessitating external shear forces for the removal of surface-attached microorganisms. Despite the potentially minimal shear force required, it remains essential for the antibacterial process. Furthermore, although the mechanical properties of structurally fortified coatings have markedly improved, their antibacterial efficacy in stagnant water environments remains insufficient due to their reliance on surface wettability for antibacterial characteristics. Consequently, an urgent need arises for an effective and environmentally friendly solution to combat fouling adhesion in stagnant water environments.

2.3 Non-toxic antifouling coating based on main chain degradable polymer

The antifouling coating incorporating the main chain degradation polymer [42] shares similarities with traditional SPC coatings. However, the key distinction lies in the degradable main chain of the former, whereas the latter can only undergo hydrolysis in the side chain. As previously mentioned, traditional antifouling coatings exhibit poor performance in stagnant water environments. The degradable polymer is synthesized through ring-opening polymerization of cyclic monomers, resulting in a main chain with degradable bonds. These cleavable bonds render the polymer susceptible to attack by seawater or enzymes in static conditions, causing degradation into small, water-soluble molecules.

Qian et al. [43] developed innovative antifouling coatings by integrating butenolide derived from marine bacteria into a biodegradable poly(ε-caprolactone) (PCL) based polyurethane matrix **(Figure 4A)**. Evaluate the antifouling performance of panels coated with

PCL–PU80/butenolide and PCL–PU80/rosin/butenolide after soaking in seawater for 3 months. After 3 months, PCL–PU80/rosin/butenolide showed the best antifouling performance **(Figure 4B)**. The degradation of the polymer enables a self-renewing surface and functions as both a carrier and release system for butenolide. **Figure 4C** shows the time-dependent release rate of butenolide at different concentrations. The release rate varies with the concentration of butenolide and is positively correlated with the concentration of butenolide in PCL-PU80. The release rate of the antifouling agent can be effectively controlled by adjusting the concentration of butenolide. To enhance the long-term release rate, rosin was introduced into PCL-PU80. The inclusion of rosin enhances the self-polishing rate and improves the delayed release of butenolide in biodegradable polymers **(Figure 4D)**.

Jiang et al. [44] conducted a separate study to develop highly branched copolymers for antifouling coatings, wherein the main polymer chains are interconnected by degradable fragments of PCL **(Figure 4E)**. **Figure 4F** presents the results of algicidal adhesion tests. The control panel exhibits approximately 60% coverage by phaeodactylum tricornutum. However, when the surface is coated with copolymers containing varying CL contents (ranging from 27% to 39%), the adherence of phaeodactylum tricornutum decreases from 24.45% to 4.74% **(Figure 4G)**. This reduction is attributed to the formation of a dynamic surface resulting from the degradation of the PCL fragment bridges, which contributes to the excellent antifouling ability. The mentioned novel design of a polymer with a self-renewing surface plays a crucial role in determining the performance of the degradable polymer and provides insights for the subsequent design of polymers with degradable main chains and hydrolyzable side chains.

Main chain degradable polymers can undergo decomposition or chemical hydrolysis by microorganisms, leading to the production of small molecules or low molecular weight substances. This process mitigates the accumulation of microplastics in the ocean, and the continually evolving surface properties ensure persistent antifouling capabilities. However, the anti-biofouling effectiveness of degradable polymers exhibits an inverse relationship with ester density and hydrophilicity but correlates negatively with crystallinity [45]. This behavior contradicts the response observed in mechanical properties, thereby creating a narrow range

for regulating the degradation and mechanical attributes of degradable polymers. Furthermore, the functionalization or chemical modification of degradable polymers presents formidable challenges. Cyclic monomers, in particular, frequently lack the functional or modifiable groups necessary for stabilizing their cyclic structures [46]. Consequently, the availability of functional cyclic monomers is limited, rendering the synthesis of cyclic monomers with modifiable groups a challenging endeavor.

2.4 Non-toxic antifouling coating based on main chain degradation and branch chain hydrolysis polymer

Degradable and hydrolyzable polymers, also referred to as "degradable vinyl polymers", offer a promising alternative to main chain biodegradable antifouling coatings. As discussed earlier, the application of main chain biodegradable coatings is limited due to challenges associated with functionalization and chemical modification. In contrast, vinyl polymers provide several advantages, including controllable degradation and improved mechanical properties [42, 47]. Moreover, the ability to incorporate functional side groups from vinyl monomers and polyester segments from cyclic monomers into a single polymer chain through polymerization facilitates easier functionalization of vinyl polymers. Therefore, vinyl polymers offer a more practical and effective approach for achieving both controllable degradation and convenient functionalization compared to main chain biodegradable antifouling coatings.

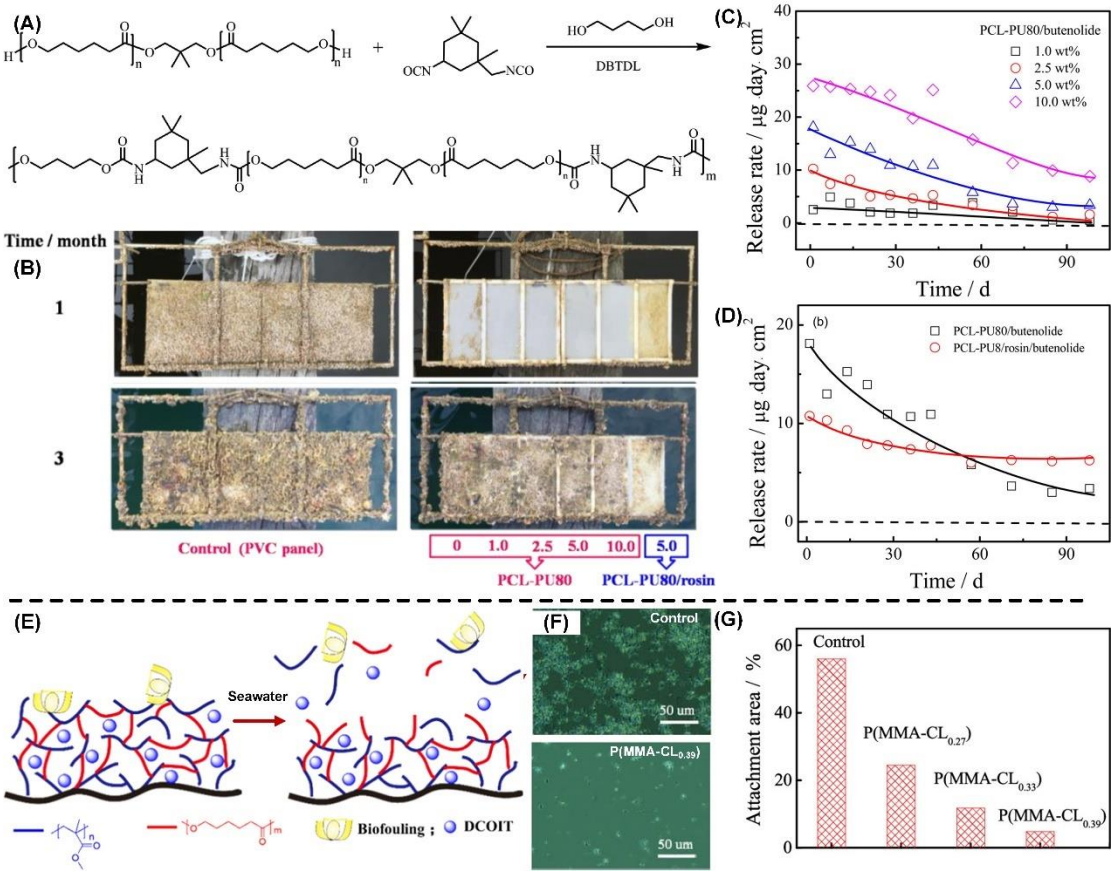

Figure 4 (A) Synthesis of PCL-Based Polyurethane. **(B)** Field test of PCL–PU80/butenolide and PCL–PU80/rosin/butenolide coatings after 3 months. **(C)** Time dependence of release rate of butenolide from biodegradable PCL–PU80. **(D)** Time dependent release rate of butenolide from PCL–PU80 and PCL–PU80/rosin. **(E)** A schematic diagram illustrating the antifouling mechanism of the degradable coating on the main chain. **(F)** Optical microscopy images capturing the settlement of Phaeodactylum tricornutum on the coating surface and blank control group over a 14-day period. **(G)** Attachment area of phaeodactylum tricornutum settled on the surface of the coated copolymers with different CL contents for 14 days.

For instance, degradable and hydrolyzable hyperbranched polymers were synthesized by copolymerizing methacrylic anhydride through reversible addition-fragmentation chain transfer polymerization (RAFT) [48]. As depicted in **Figure 5A**, when in contact with the surface or seawater, the polymer undergoes hydrolysis and degradation, resulting in the formation of short segments that constitute a dynamic surface. The hydrolysis of tertiary carboxybetaine ester acrylate with the antifouling group N-(2,4,6-trichlorophenyl)maleimide (TCB-TCPM) generates antifouling groups TCPM (killing) and zwitterionic groups (resistance). This polymeric coating demonstrates a controlled degradation rate, which is

enhanced by increasing the degree of branching. Antibacterial tests conducted after immersing the coating in artificial seawater (ASW) for 14 days revealed a consistently low presence of biofilms **(Figure 5B)**. The polymers containing TCB-TCPM groups exhibited exceptional antifouling properties.

Furthermore, a marine antibacterial scaling material with excellent drag reduction and adjustable self-polishing rate has been developed [49]. This material consists of a polyurethane matrix composed of PCL main chain segments and poly(triisopropylsilyl acrylate) (PTIPSA) side chains, prepared through a combination of radical polymerization and condensation reaction **(Figure 5C)**. In extensive marine field tests lasting 90 days, the polyurethane material demonstrated exceptional cleanliness and resistance to fouling **(Figure 5D1)**. (Polyurethane with PTIPSA side chains is designed as PU-S_x, where x is the weight percentage of PTIPSA estimated by ^{1}H NMR.) The synergistic effect of the combined system resulted in significantly enhanced antifouling performance, even in static marine environments **(Figure 5D2)**. This improved performance can be attributed to the self-renewing nature of the polyurethane coating, facilitated by the biodegradable PCL main chain and hydrolyzable PTIPSA side chains.

Feng et al. [50] introduced a zwitterion hydrogel coating that forms an interpenetrating network with polymer substrates **(Figures 5E1, 5E2)**. The hydrogel coatings, composed of zwitterionic polysulfobetaine methacrylate (PSBMA), effectively prevented bacterial adhesion on the substrates. The presence of gentamicin sulfate (GS) enabled the release of antibacterial agents triggered by the weakly acidic environment created by bacterial metabolism. Furthermore, hyaluronidase secreted by the adhered bacteria facilitated the degradation and detachment of the bacterial-adhering sites, leading to the removal of bacteria and the renewal of antifouling surfaces. These novel designs above, incorporating main chain degradation and side chain hydrolysis, significantly contributes to the performance of non-toxic antifouling coatings and offers insights for the future development of antifouling coatings with robust mechanical stability.

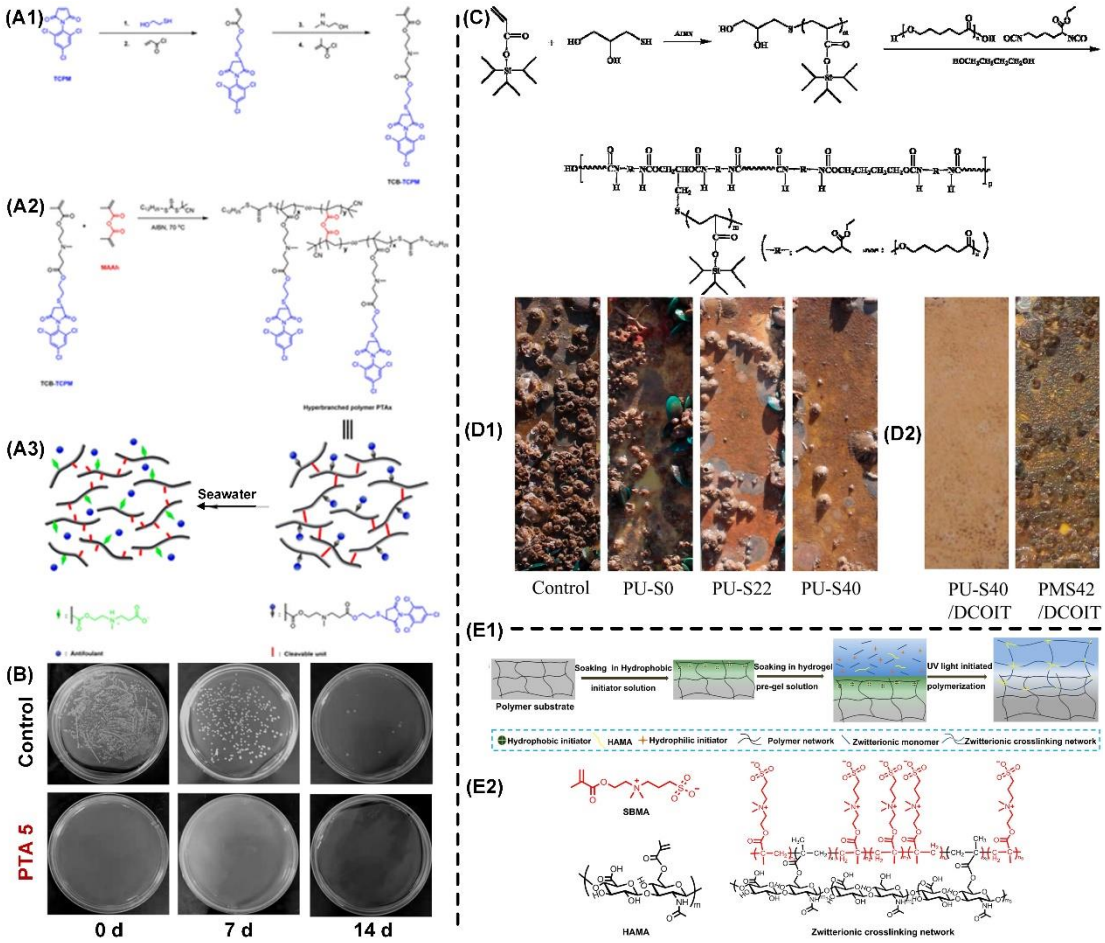

Figure 5 Synthesis of (A1) TCB-TCPM and (A2) PTAx and (A3) hydrolysis and degradation of PTAx. (B) Distribution of bacteria after PTA5 and uncleavable divinyl monomer EGDMA (ethylene glycol dimethacrylate) immersion in bacterial suspension in ASW for different time. (C) Synthesis of degradable polyurethane with hydrolyzable side chains. (D1) Panels coated with PU-Sx. (D2) Panels coated with PU-S40 and PMS-42 in combination with DCOIT (10 wt%) after immersion in seawater for 3 months. (E1) Schematic representation of the zwitterionic hydrogel coating preparation process. (E2) Chemical structure of SBMA, HAMA, and zwitterionic cross-linking network

These novel designs above, incorporating main chain degradation and side chain hydrolysis, significantly contributes to the performance of non-toxic antifouling coatings. The rate of polymer degradation can be precisely controlled by modifying the structure of polymers with degradable main chains and hydrolyzable side chains. Remarkably, even in stagnant water environments, these coatings exhibit outstanding antifouling capabilities. However, this category of antifouling coating is constrained by the inherent strength of the polymer, posing challenges for ensuring long-term durability. Consequently, the focal point of the next

generation of marine antifouling materials revolves around the introduction of cross-linked networks and armor-like microstructures to enhance the mechanical properties of coatings while preserving their original performance. Antifouling coatings featuring degradable main chains and hydrolyzable side chains offer valuable insights for the future development of coatings with robust mechanical stability. These coatings are expected to assume a pivotal role in the realm of marine biological pollution prevention.

3. Properties of non-toxic antifouling coatings

3.1 Antifouling property

3.1.1 Protein fouling

Proteins are biological macromolecules composed of amino acids, and non-specific protein adsorption can occur on almost all surfaces in direct contact with protein containing environments [51]. This phenomenon is a very challenging problem for many marine vessels and biomedical applications. Protein adsorption is the first step **(Figure 1E)** in triggering the attachment of biological fouling, so anti-protein adsorption surfaces are expected to reduce the accumulation of fouling. Poly(ethylene glycol) (PEG) and Zwitterion polymers are widely used in marine antifouling field due to their excellent protein resistance. By hydrogen bonding or electrostatic induced interactions with water molecules, the formation of hydration layer on the surface to achieve strong antifouling ability.

Traditional PEG and its derivatives are currently the most widely used antifouling materials. Kim et al. [52] fixed water molecules onto the surface of PDA/TA through hydrogen bonding **(Figure 6A1)**, and the PDA/TA/PEG coating exhibited excellent non-specific protein adsorption on fibrinogen (The fluorescein-isothiocyanate-labeled lysozyme protein solution was added onto the wetted surface. The surface was then placed, rinsed, and examined by fluorescence microscopy after being incubated for 15, 30, and 120 min. **(Figure 6A2**). Moreover, the coating still had a certain resistance to diatoms after immersion in sea water, due to the low adhesion (0.39 ± 0.17 nN) of proteins on the surface of SAC **(Figure 6B)**, the protein tends to slide on the confined water film adsorbed on the SAC microchannel wall,

demonstrating its potential in ship antifouling applications **(Figure 6C)**. However, the high hydration of PEG materials and excessive expansion in water environments can further affect the mechanical strength of the coating, and the instability of PEG structure limits the long-term protein adsorption resistance of the coating.

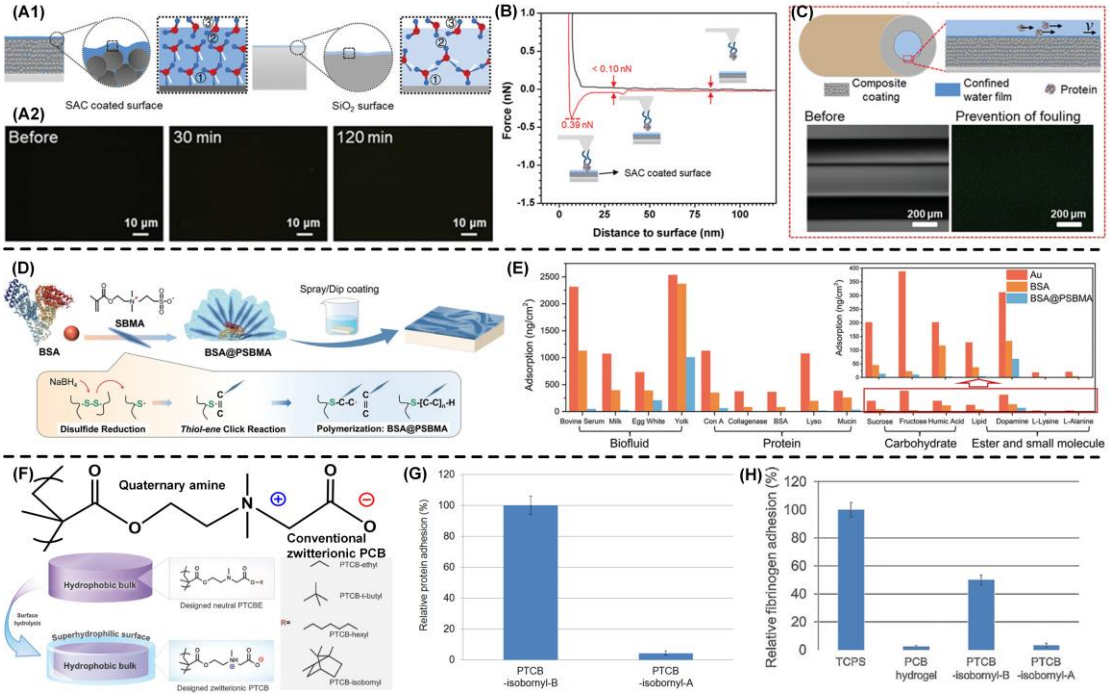

Figure 6 (A1) Schematics of the water film structures. The water molecules on the SAC surface show a strong and dense hydrogen-bonded network, whereas the water molecules on the uncoated bare silica surface are in a loose state. **(A2)** The SAC surface resisted protein adsorption on the surface. **(B)** The force–distance curve. **(C)** Migration and adhesion processes of fluorescently labeled BSA protein in coated microchannels and bare silica. **(D)** Schematic diagram showing the process of synthesizing BSA@PSBMA via thiol-ene click chemistry. **(E)** Adsorption of biofluids, proteins, carbohydrates, and small molecules on different sensors after rinsing with water. **(F)** Schematics of non-fouling PTCBE elastomer. **(G)** Protein adhesion on PTCB-isobornyl-A (after hydrolysis of 110 hours) was normalized to that of PTCB-isobornyl-B (before hydrolysis). **(H)** Biological tests: the quantative measurements of fibrinogen for TCPS, PCB hydrogel, PTCB-isobornyl-B, and PTCB-isobornyl-A.

Zwitterion has strong hydration effect through ionic solvation, which endows the material with excellent anti-protein adsorption performance. Zhao et al. [53] grafted zwitterion sulfobetaine methacrylate (SBMA) segments onto natural BSA molecules through simple thiol-ene click reaction **(Figure 6D)**, BSA@PSBMA coating exhibited excellent resistance to proteins, enzymes, metabolites, cells, and biological fluids. The residual levels of BSA on

natural BSA coating and bare Au coating were as high as ~1131 ng·cm^{-1} and ~2313 ng·cm^{-2}, respectively BSA@PSBMA-coated Only ~50.3 ng·cm^{-2} **(Figure 6E)**. Hung et al. [54] used tertiary carboxybetaine ester polymer (PTCBE) derived from zwitterionic polycarboxybetaine (PCB) to construct a material with excellent mechanical strength and anti-scaling performance **(Figure 6F)**. The surface of PTCBE can be hydrolyzed in a controlled manner under specific conditions, forming a thin hydrated layer to resist non-specific adsorption. PTCB-isonyl-A (the fully hydrolyzed surface was expressed as PTCB-isonyl-A) and PCB hydrogels both showed excellent anti-scaling ability, and the fibrinogen adsorption capacity was 96.7% and 97.7% lower than that of tissue culture polystyrene (TCPS), respectively **(Figure 6G)**. Compared with the protein before hydrolysis (PTCB-isobornyl-B), the protein adsorption rate on the fully hydrolyzed surface was <5% **(Figure 6H)**.

3.1.2 Germ fouling

Bacteria adhere by secreting extracellular polymeric substances that anchor themselves on the surface of conditioning film and gradually develop into biofilms, mature biofilm formation is difficult to remove [55]. Ko et al. [56] proposed a dynamic magnetic response composite material that can generate coordinated undulating topographical waves with controlled length and time scales, triggering local and global eddies near the material surface, thereby removing initial pollutant attachment **(Figure 7A)**. A smaller time scale resulted in higher vorticity and greater wall shear stress, and bacterial cells near the surface have a lower chance of being in contact with the surface due to high shear, making it difficult to properly form biofilms. Higher length scale values meant that sufficient deformation of the bottom surface is required to cause large eddy currents and greater wall shear stress, and the better the scaling resistance **(Figure 7B)**. After 18 h of cultivation at 37℃, dynamic fluctuating surfaces on the time scale (3 s) and length scale (0.394 mm) showed excellent adhesion properties against *E. coli* **(Figure 7C)**.

The high hydrophilicity of zwitterion polymers makes them easy to expand when immersed in the marine environment (high salinity), which will reduce their antifouling performance and mechanical strength [57, 58]. Li et al. [59] constructed zwitterion three

network (ZTN) hydrogel with excellent mechanical properties and antifouling properties through poly(trimethylamine N-oxide) (pTMAO) and poly(sulfobetaine) (pSB) with strong electrostatic interaction and network entanglement **(Figure 7D)**. The hydrogel coating can maintain high mechanical properties in the salt environment, and show excellent anti-bacteria and cell adhesion behavior to *E. coli* bacteria and HEK-293 cells in the salt solution environment **(Figure 7E)**.

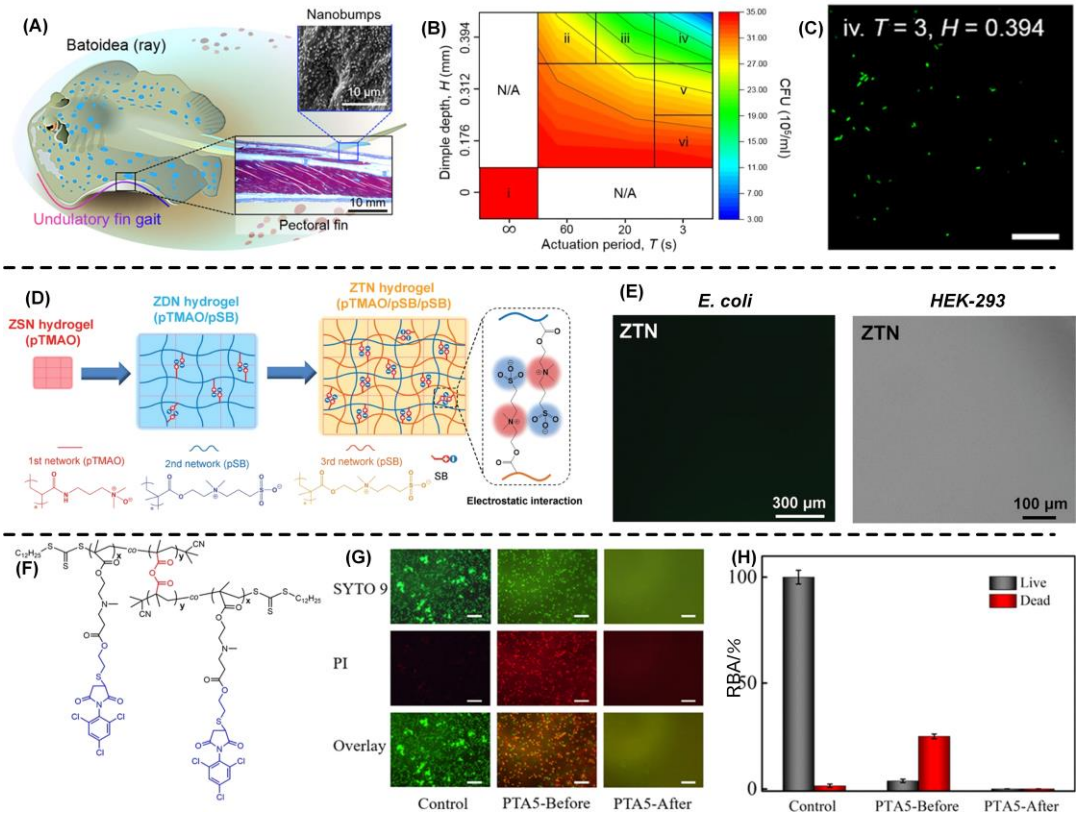

Figure 7 (A) Conceptual illustration showing the undulatory gait of the Batoidea's pectoral fin together with the histological cross section of the pectoral fin (red, muscle; blue, collagen and bone). Nanoscale bumps are observed on the surface of the pectoral fin (SEM). **(B)** Phase diagram showing different regimes of the CFU counting according to the actuation period (T) and dimple depth (H) of topographical waves. **(C)** Confocal microscopy images of the stained *E. coli* cultured on the dynamic undulatory composite surfaces with topographical waves: T=3 s and H=0.394 mm. **(D)** Schematic for preparation of the pTMAO/pSB/pSB ZTN hydrogel with strong electrostatic interaction and network entanglement. **(E)** Non-fouling tests of the ZTN hydrogel: images of *E. coli*, and HEK-293 cell adsorption on the ZTN hydrogel. **(F)** Synthesis of PTAx. **(G)** Fluorescence photographs and **(H)** relative bacterial adsorption (RBA) of Pseudomonas sp. adhered on the polymer surfaces-green color indicates all the adsorbed bacteria (SYTO 9) and red color indicates dead bacteria (PI). Scale bar: 50 μm.

Dynamic surface antifouling has received widespread attention due to its excellent surface

renewability, controllable release of antifouling agents, and long-lasting antifouling properties. Dai et al. [48] synthesized a new monomer-tertiary carboxybetaine ester acrylate with antifouling group TCB-TCPM, and through copolymerization with methacrylic anhydride (PTAx), the polymer showed a controllable degradation rate **(Figure 7F)**. The antifouling group TCPM generated by TCB-TCPM hydrolysis kills bacteria and generates zwitterion on the surface to resist bacterial adhesion. Before the hydrolysis of the coating, a large group of dead bacteria was observed on the surface, indicating that PTA5 can effectively "attack" bacteria. There are almost no bacteria on the surface of hydrolyzed PTA5, indicating that the surface of zwitterion generated after hydrolysis can effectively "prevent" bacterial cell adhesion **(Figures 7G, 7H)**.

Preventing bacterial adhesion on surfaces has emerged as a crucial approach to combat biofilm formation, a problem of significant consequence in the medical domain. The pursuit of antibacterial adhesion surfaces holds considerable promise for advancing biomedical applications.

3.1.3 Blood fouling

The construction of anti-blood adhesion surfaces is crucial for medical devices, thrombus formation usually causes inflammation and infection [60]. Nokes et al. [61] used a high throughput roll to roll manufacturing method to prepare superhydrophobic surfaces (SH) by shrinking pre-stressed thermoplastic materials with thin and hard silver and calcium layers **(Figure 8A)**. (i) Silver is first deposited, (ii) then calcium is deposited in sheet evaporation. (iii) The SH features are formed while shrinking the metalized film, and the SH features are (iv) molded into an intermediary silicone and (v) embossed into plastic to achieve the final product. Still images of blood sliding on flat and SH PP are taken with a high-speed camera. High contact angle and low contact angle hysteresis demonstrate excellent anti-blood adhesion. Blood can slide off the superhydrophobic surface within 0.25 s without any residue **(Figure 8B)**. The residual area of blood on the flat surface was 21% ± 5%, while the SH surface was only 0.005% ± 0.004 **(Figure 8C)**.

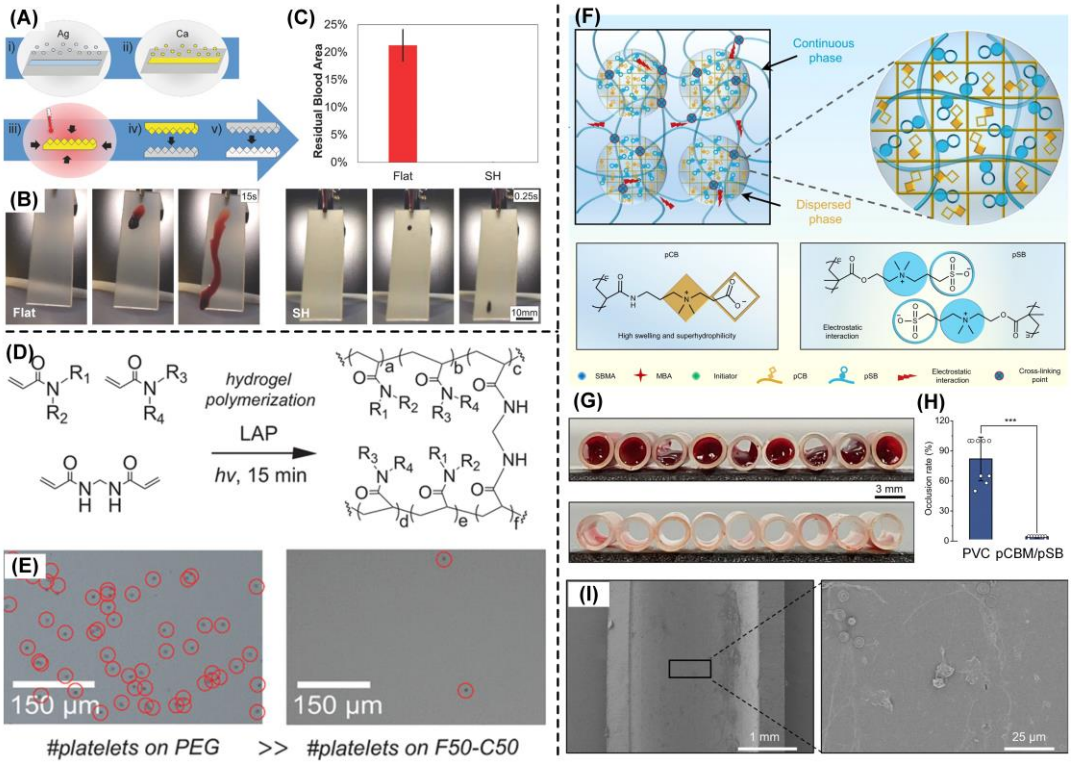

Figure 8 (A) Preparation of superhydrophobic surfaces by shrinking pre-stressed thermoplastic materials with silver and calcium layers. **(B)** Optical image of blood sliding off a flat and SH surface. **(C)** Blood residue area is reduced >4200× on the SH surface compared to flat. **(D)** Photopolymerization of anti-biofouling acrylamide-based hydrogels combinations. **(E)** Anti-biofouling performance of copolymer hydrogels to platelet. **(F)** Network structure and the preparation process of the pCBM/pSB hydrogel. Cross-section **(G)** of pCBM/pSB hydrogel coating modified PVC tubing after 2 h of circulation. The quantitative results of **(H)** occlusion rate. SEM images of **(I)** pCBM/pSB hydrogel coating modified PVC tubing after 2 h of circulation.

Chan et al. [62] used a high-throughput screening method to evaluate the biological pollution performance of 11 combined copolymer hydrogel materials assembled from 172 different acrylamide-based monomers **(Figure 8D)**. The 50:50 copolymer of hydroxyethyl acrylamide and diethyl acrylamide (F50-C50) exhibits much lower platelet adhesion than PEG (Hydrogel samples were first incubated in 50% fetal bovine serum for 24 h at 37°C to ensure extensive protein adsorption to the samples. Platelet rich plasma (PRP) obtained from centrifugation of rat blood was then incubated on the surface of the hydrogels for 1 h at 37°C. Several polyacrylamide copolymer hydrogels presented significantly less platelet adhesion than PEG, PHEMA, and polyzwitterionic hydrogel controls. **(Figure 8E)**. The high-throughput

screening method provided guidance value for the application of polyacrylamide-based polymer coatings in anti-biofouling materials.

Zwitterionic polymers are ideal materials to prevent thrombosis due to the superhydrophilic characteristics of their equal positive and negative charges on the same side of the chain [63, 64]. Yao et al. [65] prepared poly(carboxybetaine) microgel (pCBM) reinforced pSB Zwitterion hydrogel as a coating for blood contact prevention devices **(Figure 8F)**. Compared with the original PVC tube, which formed a large number of thrombi and caused obvious occlusive thrombosis (82.0 ± 21.7%), the pCBM/pSB hydrogel coating modified PVC tube had almost no detectable occlusion (4.3 ± 1.3%) **(Figures 8G, 8H)**. Only a few platelets and red blood cells were observed on the surface of pCBM/pSB hydrogel coating **(Figure 8I)**. Blood coagulation and infection present notable challenges in the utilization of clinical medical devices like catheters and vascular stents. The design of anti-blood adhesion surfaces holds the potential to mitigate blood adhesion and diminish the risk of infection, thereby exerting a substantial influence on an array of medical instruments.

3.1.4 Incrustant fouling

The formation of scale can cause a loss of efficiency during energy transportation, leading to serious heat transfer impacts [66]. Traditional methods based on physical removal, magnetic field, electronic field, and ultrasound face problems such as high cost, high energy consumption, and significant environmental pollution. At present, the construction of advanced anti-scaling interface materials, such as superhydrophilic surfaces, superhydrophobic surfaces, and liquid injection surfaces, has shown enormous potential applications in the field of anti-scaling [67, 68]. Huang et al. [69] studied the surface hydration of polytrimethylamine N-oxide polymer brushes (pTMAO) and the effects of salts and proteins on this surface hydration **(Figure 9A)**. The excellent salt resistance was due to the short distance between positively charged and negatively charged groups, so the dipole in pTMAO was small, and TMAO Zwitterion showed strong hydration. The atomic MD results verified the strong hydration of pTMAO surface in water and 0.6 M NaCl solution, demonstrating effective resistance to salt and protein induced

damage (The inset shows the equilibrated pTMAO/water interface. Red beads represent water molecules within the first hydration shell (i.e., the cutoff distance is up to the valley of pG(r) indicated with a black arrow). The bulk water is colored gray. Na^+ and Cl^- ions are represented with red and green beads, respectively. The surface density is 2.4 TMAO chains/nm^2, and the repeating unit (n) is 4. **Figures 9B, 9C**).

Superhydrophobic coatings can achieve excellent surface anti-scaling performance by reducing the nucleation density and growth rate of $CaCO_3$ crystals, controlling the shape of the crystals (i.e., needle-like aragonite). Qian et al. [70] prepared superhydrophobic polyphenylene sulfide (PPS)/polytetrafluoroethylene (PTFE) composite coatings **(Figure 9D)**. Compared with commercial hydrophobic EP silicone resin coatings, superhydrophobic PPS/PTFE composite coatings show unique anti-scaling performance. Due to the synergistic effect of morphology and low surface energy, the superhydrophobic PPS/PTFE composite coating exhibits three different scaling morphologies (flaky rhombic crystals, globular villous clusters, and nanoscale needle clusters) **(Figure 9E)**. The deposition rate of $CaCO_3$ on the superhydrophobic PPS/PTFE coating is only 38.6% of that on the EP silicone resin coating **(Figure 9F)**, indicating excellent anti-scaling performance.

The anti-scaling performance of SLIPS is mainly due to the reduced nucleation rate of salt on the surface and the low adhesion strength between scale and SLIPS. Yao et al. [71] developed a scale resistant smooth lubricant induced surface (HTS-SLIPS) through one-step electrodeposition and lubricant injection **(Figure 9G)**. The cube calcite-like scale was processed by false color in yellow, and the needle-shaped aragonite scale was depicted in false color blue. The unmodified SS304 had Ca content of up to 33.94 wt%, while the Ca content on HTS-SLIPS was only 4.46 wt% **(Figure 9H)**. The cumulative scale mass on HTS-SLIPS soaked in boiling salt water was the lowest, at 2.25 $mg \cdot cm^{-2}$ **(Figure 9I)**, demonstrating the significant stability of the smooth coating in anti-scaling under harsh conditions. The formulation of anti-incrustant surfaces offers an effective resolution to high energy consumption and the latent safety risks, offering viable remedies for intricate settings within the petroleum transportation and chemical industry domains.

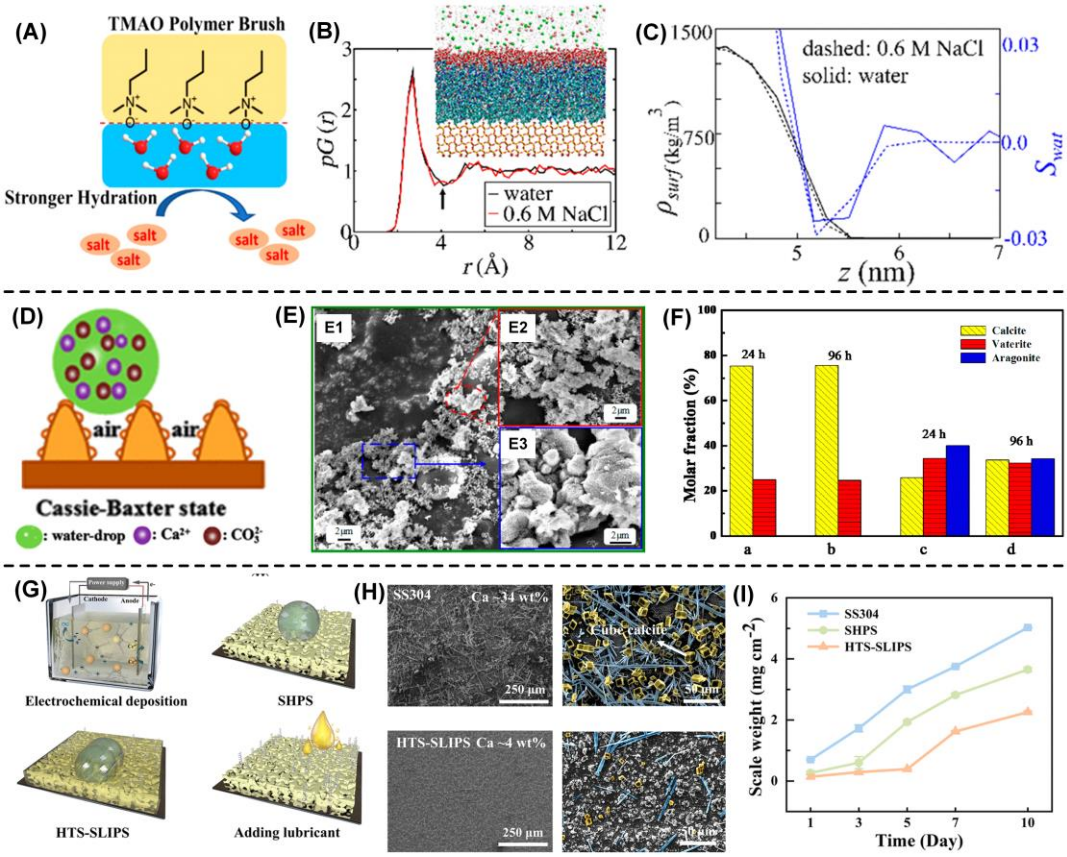

Figure 9 (A) The surface hydration of TMAO polymer brushes (pTMAO). **(B)** pG(r) of a pTMAO surface in the water and 0.6 M NaCl solution, drawn using the final 20 ns MD simulation data. **(C)** Densities of pTMAO (black) and water ordering parameter S_{water} as a function of position across the pTMAO/water interface calculated by MD simulation (solid line, the system with pure water; broken line, the system with 0.6 M NaCl). **(D)** Antifouling mechanism of the superhydrophobic PPS/PTFE composite coating. **(E)** SEM images of $CaCO_3$ scaling on the superhydrophobic PPS/PTFE composite coating with different soaking times: 24 h. **(F)** Relationship between the surface energy and $CaCO_3$ scaling weight at the hydrophobic EP–silicone coating and the superhydrophobic PPS/PTFE coating after testing with 360 h at 60°C. **(G)** Schematics illustrate the fabrication process of pitcher plant-inspired HTS-SLIPS. **(H)** Top-view SEM images of scale distribution on the samples with corresponding Ca element concentration from EDS characterization. **(I)** The scale weight change of different samples with time in a 10-d scaling test.

3.1.5 Anti-ice and anti-fog

The phenomenon of fogging has brought many inconveniences to our daily production and life, directly or indirectly causing huge economic losses [72]. Wettable anti-fogging coatings have become a research hotspot due to their simple preparation, low cost, and easy maintenance [73, 74]. Anti-fogging coatings are mainly divided into two categories in terms of wettability:

hydrophobic and hydrophilic. Water droplets have low adhesion on the surface of hydrophobic coatings and can be easily removed from the surface under external forces. Hydrophobic coatings have advantages in long-term effectiveness [75]. Water diffuses on the surface of the hydrophilic antifogging coating to form a water film to achieve anti-fogging effect, and the hydrophilic coating usually faces the problem of anti-fogging effectiveness due to the easy adhesion of fouling [76].

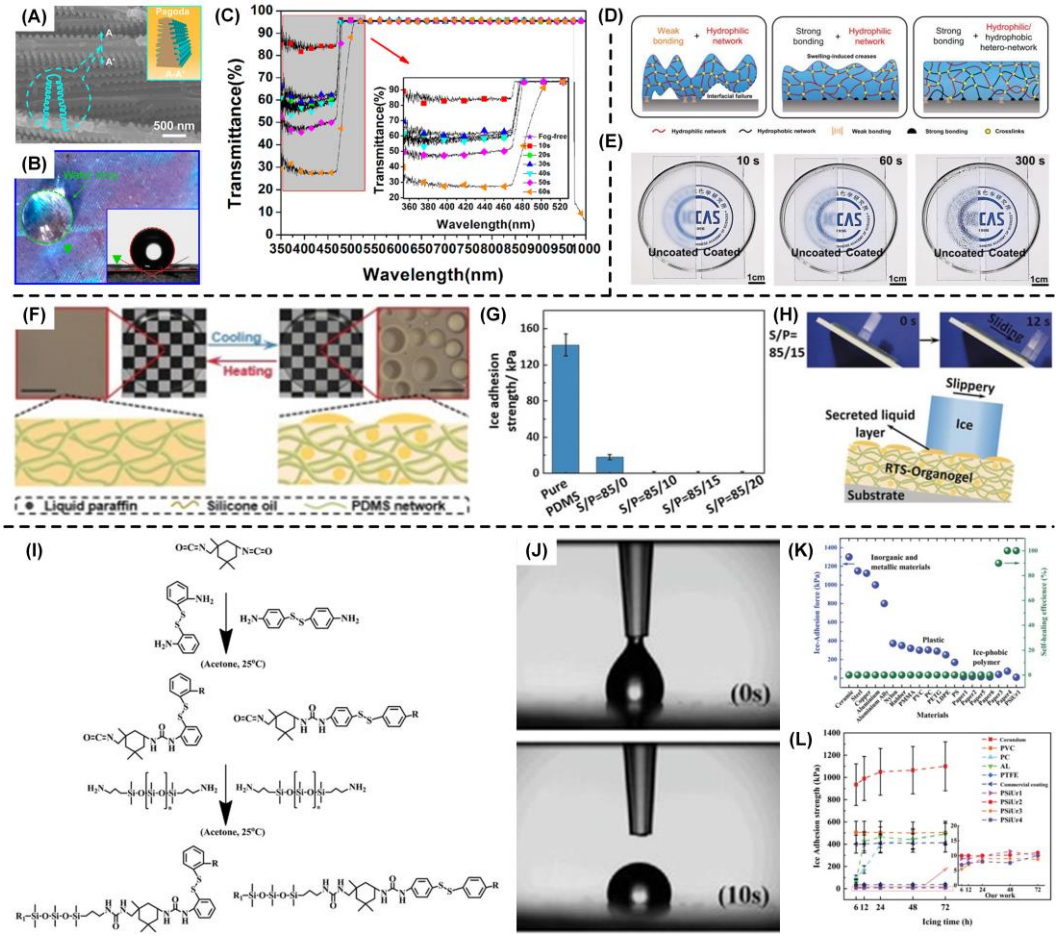

Figure 10 (A) FESEM image of the biomimetic pagoda structure (inset) from the side view under high magnification. **(B)** Digital photo and CA measurement image (inset) of the wing surface (green triangle) show excellent superhydrophobic property. **(C)** Core components of the self-built spray simulation system and transmittance spectra of the glass substrate and MHPS-based BMF. **(D)** Design of the thick hydrophilic/hydrophobic polymer hetero network coating for effective antifogging performance. **(E)** Antifogging behavior of uncoated and the one coated with PVA/PTPM HN in 60℃ for different times. **(F)** Phase separation of the RTS-organogel. Scale bar, 50 μm. **(G)** The ice adhesion strength of different samples at -15℃. **(H)** Sliding process of ice pillar on the surface of the RTS-organogel at -15℃. And schematic illustration of the anti-icing mechanism. **(I)** The flow diagram of synthesis of PSiUr materials. **(J)** Surface contact performance of water droplets of PSiUr1. **(K)** Comparison of ice adhesion

strength of different reported commercial materials. **(L)** The ice adhesion strength of different substrates, commercial coating, and PSiUr after icing at different hours.

Inspired by butterfly wing scales, Han et al. [77] successfully prepared SiO_2 biomimetic monolayer (BMF) **(Figure 10A)** through simple sol-gel method and selective etching process, BMF exhibited significant superhydrophobicity **(Figure 10B)**. It can maintain high light transmittance (~95%) under the condition of 0.5 $mL \cdot min^{-1}$ spray, and can almost immediately return to the fog free state (<5 s) **(Figure 10C)**.

Shi et al. [78] realized long-term antifogging performance by thickening the strong adhesive coating of hydrophilic/hydrophobic polymer heterogeneous network composed of hydrophilic polyvinyl alcohol (PVA) and hydrophobic poly (3-(trimethoxysilyl) propyl methacrylate (PTPM). Hydrophilic/hydrophobic polymer heterogeneous network coating can achieve long-lasting anti-fogging performance. The hydrophobic part in heterogeneous networks suppresses the formation of large-scale unevenness by preventing any local excessive expansion of hydrophilic polymer segments, thereby maintaining long-term anti-fogging performance **(Figure 10D)**. The 100 μm thick PVA/PTPM HN coating showed continuous fog resistance, remaining clear for at least 60 s in a 300℃-water bath, while the uncoated slides became blurred even at 10 s **(Figure 10E)**.

Ice formation is a common natural phenomenon, but the accumulation of ice can pose safety hazards to infrastructure or equipment such as power grid, ships, aircraft, and roads [79]. Based on the liquid repellent surface with passive and active anti-ice ability, it can significantly inhibit the ice core to prevent frost and reduce the ice adhesion force [80]. Ru et al. [81] designed a reversibly thermosecreting organogel (RTS-organogel) by mixing binary liquid mixture (silicone oil and liquid paraffin) with upper critical solution temperature (UCST) into the PDMS network to achieve reversible adjustment of lubrication and adhesion performance. The RTS-organogels can secrete droplets at low temperature and reversibly absorb droplets when temperature raises **(Figure 10F)**. The organic gel had a relatively low ice bonding strength (less than 1 kPa) **(Figure 10G)**. The ice pillar forming on the RTS-organogel gel can quickly slide down within 15 s at a small angle **(Figure 10H)**. Due to the presence of droplets

rich in paraffin, the actual contact area between ice and surface was lower than the apparent area, thereby reducing the adhesion strength of ice.

Chen et al. [82] prepared a polymer **(Figure 10I)** based on poly-silicone-urea, in which the amino organosilicon segment enhances the activity of the polymer chain and endows it with hydrophobic behavior **(Figure 10J)**, which is beneficial for reducing ice adhesion. Inorganic materials show ice adhesion strength over 800 kPa. The polymer (PSiUr) exhibits an extremely low ice adhesion strength of 7 ± 1 kPa. The comparison of ice adhesion strength with metal materials, inorganic materials, polymers, and reported materials shows that PSiUr materials typically have lower ice adhesion strength **(Figures 10K, 10L)**.

3.2 Adhesive property

Strengthening the adhesion between the coating and the substrate is crucial for improving its robustness and durability [83]. Through covalent bonding, crosslinking and adhesive layer assistance, the bonding strength of the surface coating and substrate interface is enhanced to obtain the coating with excellent performance [13]. Peng et al. [84] report a polyethyleneimine/thioctic acid (PEI/TA) coacervate-derived hydrogel, which can achieve robust bulk adhesion on various wet and underwater substrates **(Figure 11A)**. When PEI/TA condensates come into contact with underwater or wet substrates, they can effectively repel interfacial aqueous solutions and diffuse into the surface irregularities of the substrate, The amine group and carboxylic acid group in PEI and the 1, 2-dithianes and alkyl chain group in TA can form hydrogen bond, electrostatic interaction and hydrophobic interaction with the functional groups on the substrate surface to achieve close interface adhesion. The condensation layer then solidification into the hydrogel, increasing cohesion and establishing a stronger adhesion. PEI/TA coacervate-derived hydrogel can seal wounds and leaking plastic bottles, showing strong wet adhesion **(Figure 11B)**.

Kim et al. [85] obtained a multi-amphoteric electrolyte coating with excellent interfacial adhesion and excellent stain resistance using gas phase method. The coating consists of bilayer poly(1,3,5,7-tetramethyl-1,3,5,7-tetravinylcyclotetrasiloxane) (pV4D4) and polyampholytic

electrolyte poly(2-carboxyethyl acrylate-co-2-(dimethylamino)ethyl acrylate) (pCD) **(Figure 11C)**. Highly cross-linked pV4D4 serves as an adhesion promoter layer and can be used for various substrate materials with high interfacial adhesion. It exhibited excellent interfacial adhesion performance **(Figure 11D)** to various substrates and still exhibits excellent antifouling performance after 7 days of continuous water flow impact **(Figure 11E)**.

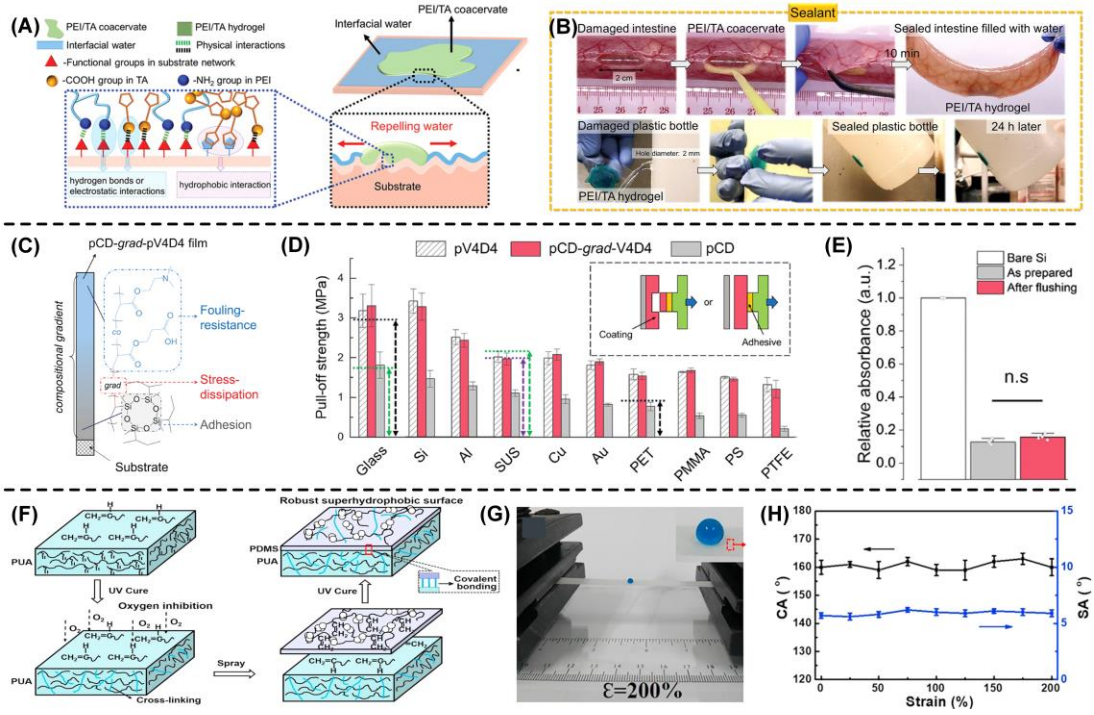

Figure 11 (A) Schematic illustration of the putative underwater adhesion mechanism of PEI/TA coacervate-derived hydrogel. **(B)** The PEI/TA coacervate-derived hydrogel can effectively seal a damaged porcine intestine in vitro (top) and a leaky plastic bottle filled with water (bottom). **(C)** A schematic representation of the pCD-grad-pV4D4. **(D)** Pull-off strength of a 100 nm thick pCD-grad-pV4D4 film on various substrate materials and test schematic diagram. **(E)** Seven days exposure to perpendicular water flush. **(F)** Schematic illustration for fabricating a mechanically stable superhydrophobic coating on stretchable substrate by UV curing. **(G)** Photographs of 10 μL water droplets (dyed with blue) maintaining their spherical shape on superhydrophobic surface at strain of 200%. **(H)** CAs and SAs of superhydrophobic coatings built on the TPU substrate at various stretching strains.

Li et al. [86] prepared a robust and stretchable superhydrophobic surface by quickly cross-linking a superhydrophobic antifouling coating (based on PDMS/silica composite material) onto the substrate using UV cross-linking **(Figure 11F)**. The covalent crosslinking formed between the superhydrophobic coating and the polyurethane acrylate (PUA) substrate was

beneficial for their interfacial adhesion. The excellent interfacial adhesion between the coating and the substrate was beneficial for improving the mechanical durability of the superhydrophobic coating on the substrate. After 1000 cycles of tensile release (strain 200%), the superhydrophobic surface maintained its original superhydrophobicity **(Figures 11G, 11H)**.

3.3 Self-healing property

The scratches and damage that antifouling coatings inevitably suffer during long-term use, leading to the loss of their antifouling function. Therefore, coatings with self-healing ability are very important for improving the stability of material use [87].

Self-healing antifouling coatings are usually divided into three types: based on surface structure rearrangement [88], based on reversible covalent [89, 90] and non-covalent interactions [91, 92], and based on reactive materials. Surface structure rearrangement is the process of repairing cracks or scratches by exposing damaged areas to solvents or heat, resulting in the rewinding and diffusion of polymer chains. Kuroki et al. [93] crosslinked poly(2-vinylpyridine) (P2VP) thin films through quaternization reaction, and grafted halogen-terminated PEO onto P2VP thin films. When surface damage occurs, changes in the free energy of PEO on the surface and network drive the rearrangement of internal PEO chains, supplementing the damaged PEO chains on the surface **(Figure 12A)**. This type of self-healing material mainly relies on the migration or rearrangement of functional polymer chains, and the thickness of such coatings is usually only a few nanometers, making it difficult to achieve significant damage healing.

The layer-by-layer (LBL) assembly method of alternately depositing polyelectrolytes or polyelectrolyte composites with opposite charges is widely used to prepare self-healing coatings. The coating thickness can be adjusted by changing the parameters during film deposition. The micron thick LBL assembled polyelectrolyte self-healing film is endowed with antifouling performance. Chen et al. [94] prepared a self-healing antifouling film through LBL assembly of PEGylated branched poly(ethylenimine) (bPEI) and hyaluronic acid (HA) **(Figure 12B)**. Due to the presence of grafted PEG, the prepared film can effectively resist protein

adsorption and cell adhesion. Cuts and scratches on the coating can achieve rapid and multiple healing after immersion in a physiological salt solution, and the healed coating still has excellent anti-cell adhesion performance.

Reaction based materials need external stimulation to trigger the reaction and regain the antifouling function. Wu et al. [95] used in situ polymerization in oil-in-water emulsion to successfully prepare various reactive or nonreactive liquid cores in in resorcinol-modified poly(urea-formaldehyde) (PUF) microcapsules (MCs) **(Figure 12C)**. When MCs containing hexamethylene diisocyanate (HDI) as a moisture-sensitive healant are dispersed in a polymer matrix, HDI can form polyurea in the presence of water to fill cracks. The occurrence of damage or defects in coatings during their application is an unavoidable reality. The self-healing capabilities of antifouling coatings not only serve to prolong the service life of antifouling materials but also mitigate economic losses attributed to the necessity of coating replacement.

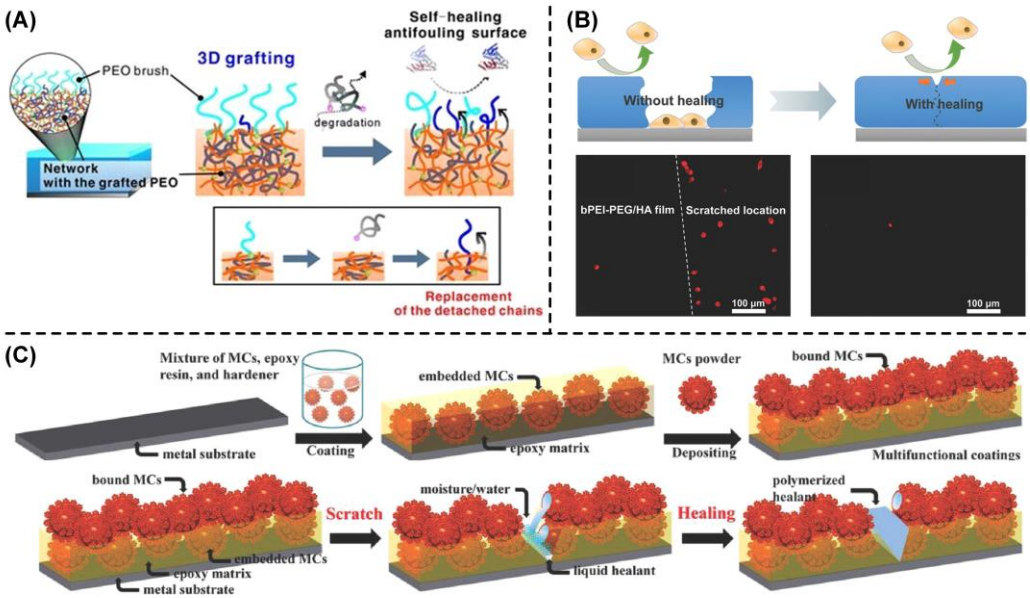

Figure 12 (A) Schematic illustration of the PEO-grafted P2VP network films: 3D polymer grafting on the surface and inside of a P2VP film. The self-healing aspect of the antifouling property is due to the rearrangement of internally grafted polymers to the interface (marked as dark blue chains). **(B)** Schematic of the damage and healing process of healable antifouling films. Cell adhesion on the scratched (left and bottom) and healed (right and bottom) c-(bPEI-PEG/HA) × 40.5 films. **(C)** Schematic of the preparing procedure of multifunctional coatings (top). And the Schematic of the self-healing process (bottom).

3.4 Electrochemical corrosion property

Steel structures in marine environments are highly susceptible to extensive corrosion due to the challenging and intricate nature of these surroundings [96]. Conventional anti-corrosion techniques, such as ultraviolet sterilization and the addition of chemical bactericides, often result in environmental contamination and substantial maintenance expenses. To address these issues, Liu et al. [97] propose an environmentally friendly approach for safeguarding steel against corrosion in seawater using a marine bacterium called Pseudoalteromonas lipolytica. This method involves the formation of a biofilm, followed by the creation of an organic–inorganic hybrid film, offering effective protection against corrosion. Among the tested strains, the EPS+ strain exhibits the most robust anticorrosion capability, as evidenced by the absence of corrosion signs even after a 15-day exposure period **(Figure 13A)**. Under the influence of EPS+, the steel surface undergoes the development of a relatively dense mineral-like film characterized by trigonal or quasi-rhombohedral structures **(Figure 13B)**. Using the diameter of the Nyquist chart obtained from electrochemical impedance spectroscopy (EIS) measurements to assess the barrier protection efficiency of different strains, the EPS+ strain provided the strongest barrier protection efficiency in the test group **(Figure 13C)**.

Ye et al. [98] dispersed functional POSS-GO fillers into an EP matrix to address initial defects, resulting in a well-performing PG/EP composite coating with long-term corrosion resistance. The anti-corrosion performance of the composite coating was evaluated using EIS after 50 days of immersion. The EIS data showed that the composite coating maintained excellent corrosion protection compared to the original EP coating **(Figure 13D)**. Potentiodynamic polarization was employed to assess the protective behavior of the composite coatings in a 3.5 wt% NaCl solution. After 50 days of immersion, the polarization data of the composite coatings were presented in **Figure 13E**. Among the coatings, the 0.5% GO/EP composite exhibited similar corrosion potential (E_{corr}=-0.69 V vs. SCE) but a lower corrosion current density ($i_{corr} = 5.48 \times 10^{-7}$ A·cm^{-2}) compared to the pure EP coating (E_{corr}=-0.67 V vs. SCE, $i_{corr} = 1.07 \times 10^{-6}$ A·cm^{-2}), indicating the best corrosion resistance. The surface of the 0.5% PG/EP composite coating appeared clear and dense, with no observable corrosion or exfoliation,

highlighting its excellent anticorrosion ability in the corrosive medium **(Figure 13F)**.

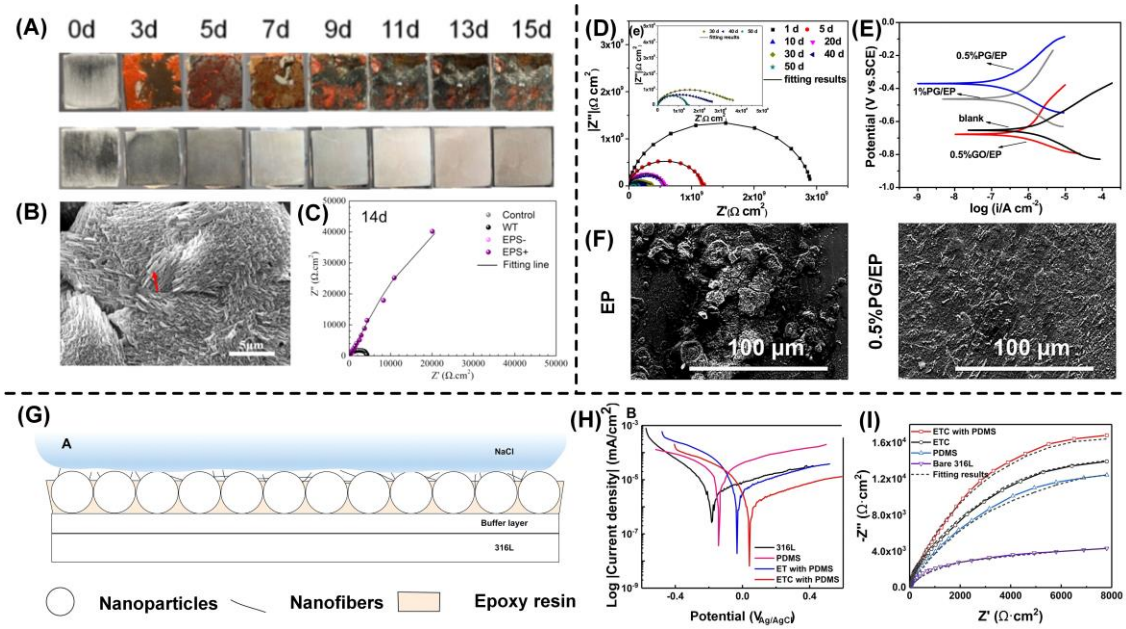

Figure 13 (A) Images of the steel surface (top: NC; bottom: EPS+) submerged in marine broth from day 1 to day 14 inoculated with three different strains. **(B)** SEM images of the steel surface (EPS+) inoculated with different P. lipolytica strains. **(C)** Nyquist plots for the steel specimens at different immersion times on day 14. **(D)** Nyquist plots of as-prepared specimens (0.5%PG/EP). **(E)** Tafel curves of all composite coatings after test. **(F)** Corrosion morphologies of all coatings after corrosion test (EP and 0.5%PG/EP). **(G)** Corrosion resistance mechanism of superhydrophobic coatings: forming an air film to avoid contact with corrosive media. **(H)** Nyquist diagram. **(I)** Bode diagram.

In recent years, there has been growing interest in superhydrophobic coatings (or surfaces) for corrosion prevention, inspired by natural plant structures and their water-repellent properties [99, 100]. These coatings utilize surface micro-nanoscale structures to create air pockets, resulting in the Cassie-Baxter wetting regime. The air layer acts as a physical barrier, effectively preventing corrosive mediums from eroding the substrate materials. Compared to traditional anti-corrosive coatings, superhydrophobic coatings with a non-infiltrating interface state (i.e., Cassie-Baxter wetting regime) exhibit higher anti-corrosive abilities by leveraging the coating's inherent self-protective properties, primarily attributed to the trapped air layer.

Zang et al. [101] developed a corrosion-resistant superhydrophobic coating by combining modified TiO_2 nanoparticles (NPs), carbon nanotubes (CNTs), and epoxy resin (EP) on a PDMS buffer layer. The micro/nano scale of the inorganic fillers and the coating material itself

contribute to its inherent hydrophobicity, impeding the penetration of corrosive solutions into the microstructure of the superhydrophobic coating **(Figure 13G)**. In comparison to the 316L steel sample, the superhydrophobic coating exhibited an increased corrosion potential in 3.5 wt% NaCl solution, shifting from -0.18 V to 0.04 V, while the corrosion current was reduced by 21 × 10^{-8} A·cm^{-2}, resulting in a lower corrosion rate **(Figure 13H)**. The EIS test demonstrated a steeper slope for the coating compared to the 316L steel substrate, indicating that the superhydrophobic PDMS layer effectively enhances the corrosion resistance of the substrate **(Figure 13I)**. These findings present novel insights for antifouling material applications in corrosive marine environments, particularly for marine equipment.

3.5 Stability

3.5.1 Mechanical stability

The coating is inevitably affected by external forces such as friction, impact, and peeling during use, and the surface of the coating will be damaged and lose its antifouling performance [102]. Therefore, durable coatings that can withstand mechanical and chemical damage are particularly important. According to the results of force, mechanical durability testing methods can be divided into tangential abrasion [13, 103], dynamic impacting [104, 105], tape peeling [106, 107], matrix deformation [108, 109], and other tests.

Circular abrasion has advantages in automation and qualitative analysis and is widely used for mechanical durability testing of surfaces. Deng et al. [110] designed a high-density, strongly cross-linked ceramic polymer superhydrophilic composite coating. After 400 Taber abrasion test, the superhydrophilic coating still had excellent anti-fogging durability **(Figures 14A, 14B)**, with a WCA of only 9.3° **(Figure 14C)**.

Sandpaper abrasion is the most common testing method used in laboratories to evaluate the mechanical durability of coatings. Usually, the coating surface is placed face down on sandpaper, and a load is applied to the solid substrate to provide pressure. Then, the substrate moves at a certain speed and distance in the tangential direction, defining lateral abrasion as a wear cycle. The degree of abrasion of sandpaper can be adjusted by the particle size of the

sandpaper, the quality of the applied load, and the distance between each abrasion cycle. Zhang et al. [111] used a suspension composed of silica micropowder, nanofumed silica, EP, and PDMS to construct a abrasion-resistant superhydrophobic coating on a variety of substrates by a simple spraying method. The coating remained in a superhydrophobic state (CA: 152°, SA: 9.7°) after being worn by sandpaper under a load of 50 g **(Figure 14D)**. After 75 times of friction (7.5 m), the SEM image did not show obvious surface finish damage **(Figure 14E)**.

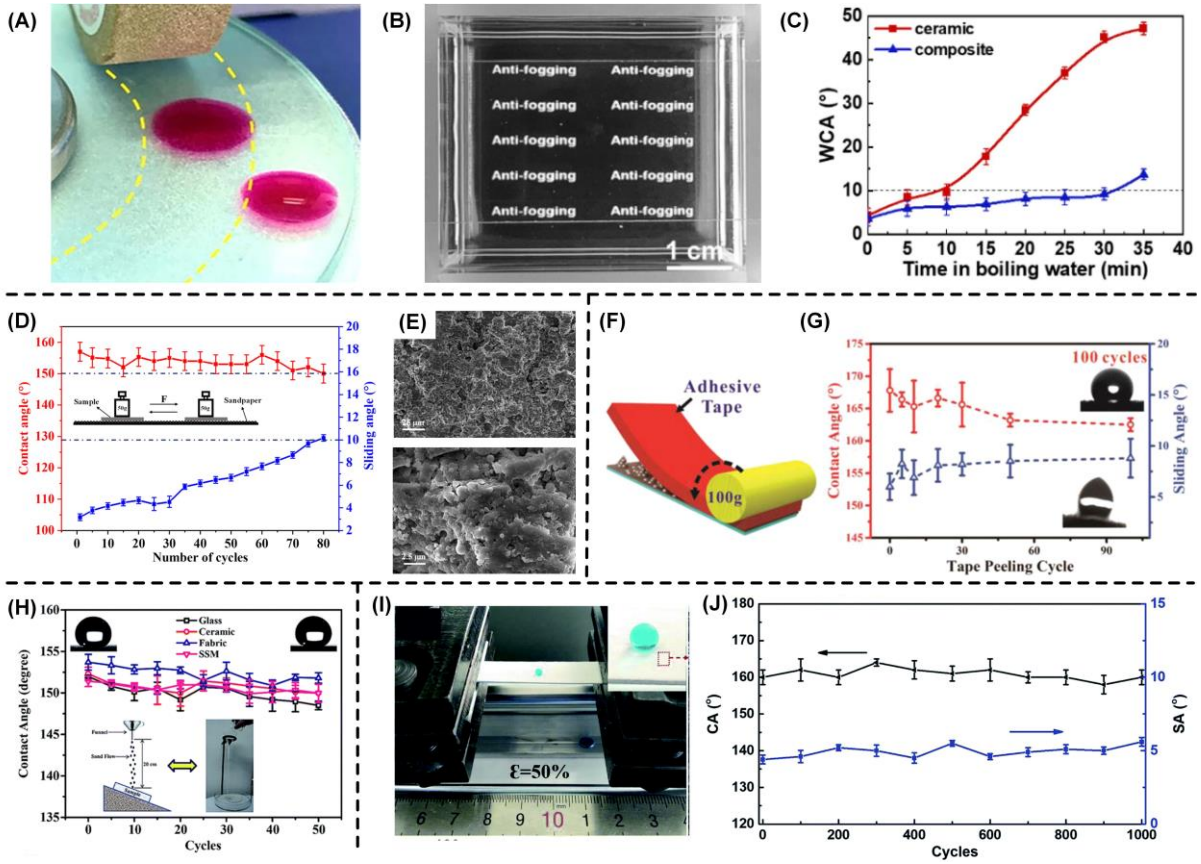

Figure 14 (A) Comparison of droplets spread (5 μL) on the composite superhydrophilic coating after 400 cycles Taber abrasion with areas without abrasion. **(B)** Comparison of anti-fogging performance for composite coating after Taber abrasion for 400 cycles. **(C)** Variation trend of WCA for ceramic and composite coating with immersion in boiling water time. **(D)** Evolutions in the CA and SA of the coated glass surface with increasing wear cycles. **(E)** SEM images of the coated glass surface after 75 sandpaper abrasion cycles. **(F)** Schematic of the adhesive tape-peeling test with 100 g on top for uniform tape-film contact. **(G)** The variation of θ_{CA} and θ_{SA} after cyclic tape peeling processes. **(H)** CA variation of AP-TiO_2@OTS coated substrates with sand impact cycles. Insets are the schematic illustration of the sand impact test. **(I)** Photographs of 10 μL water droplets (dyed with methylene blue) maintaining their spherical shape on the superhydrophobic film at strains of 50%. **(J)** CAs and SAs of the superhydrophobic film after cyclic stretching-releasing (strain of 0%→50%→0%).

Tape peeling is a commonly used method for evaluating the adhesion strength between coatings and solid substrates. As shown in **Figures 14F, 14G**, the silica NPs/microcilia array film prepared by Dai et al. [112] maintained a water contact angle of 162° and a sliding angle of 8° after 100 tape peeling cycles, demonstrating excellent superhydrophobic stability.

Laboratories commonly use methods such as sand flushing and high-speed droplet spray impact to characterize the dynamic impact resistance of coating surfaces. As shown in **Figure 14H**, Liu et al. [113] showed that 20 g of sand fell from a height of 20 cm to impact aluminum phosphate-TiO_2@aluminum phosphate coating. The coating still exhibits superhydrophobicity after 50 cycles of sand impact.

After 1000 cycles under 50% tensile strain, the PDMS/ silica film constructed by Li et al. [114] had almost no change in surface morphology before and after stretching, and still had a high WCA of 160° and a low SA of less than 5°, showing excellent mechanical stability **(Figures 14I, 14J)**.

3.5.2 Chemical stability

In addition to mechanical damage, coatings may also face surface chemical damage during use, resulting in a decline in antifouling performance [115]. Immersing the coating into different pH solutions of acid, alkali, and salt is the most extensive method for evaluating chemical stability [95]. Li et al. [116] enhanced the mechanical strength of the surface microstructure by coating a rigid aluminum dihydrogen phosphate (ADP) nanolayer on an existing fragile micro/nanostructure as a "nano-armor" layer. After immersing the coating in different pH aqueous solutions for about 24 hours, OCA and OSA remained above 160° and below 5° **(Figure 15A)**, indicating that the ADP coated surface has excellent corrosion resistance.

Zhang et al. [117] showed that after soaking in different salt solutions for 7 days, the $Cu_3(PO_4)_2$ coating can still maintain a high underwater CA of crude oil above 158° and ultra-low adhesion<3 μN **(Figure 15B)**. Even after soaking in seawater for up to 20 weeks, the membrane still exhibits stable underwater superoleophobicity **(Figure 15C)**.

Most coatings exposed to extreme temperatures can result in a loss of antifouling performance. Li et al. [118] constructed a durable superhydrophobic coating using EP modified silicone resin (MSR), functionalized SiO_2, GO, and lamellar mica powder (MP). Place the sample in liquid nitrogen for 10 min, then return to room temperature, and then place it on a hot platform at 200℃ for 10 min. This process was defined as a temperature resistant cycle. After 12 high-low temperature resistant cycles, the coating still maintained superhydrophobicity and low adhesion properties **(Figure 15D)**. The corresponding SEM images showed that significant and rapid temperature changes would not lead to cracks and evaporation degradation of the uniform and dense coating **(Figure 15E)**.

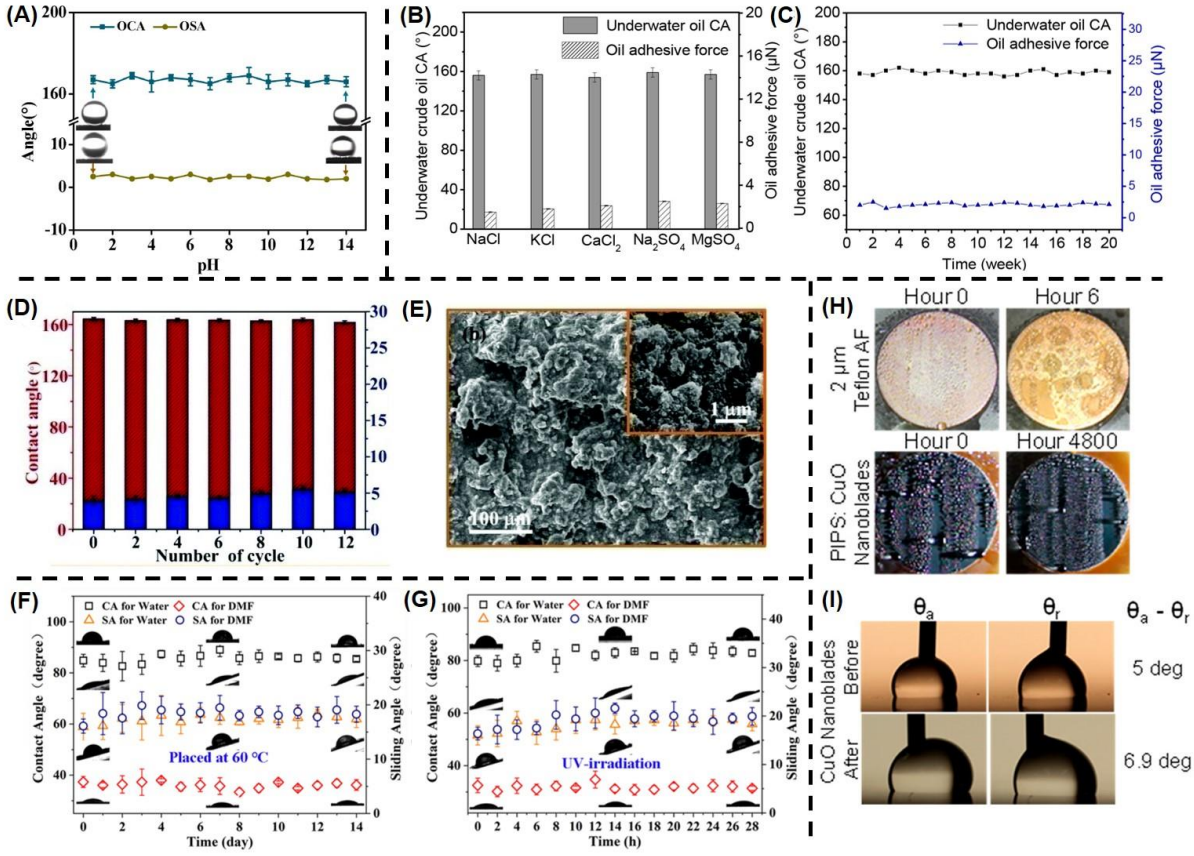

Figure 15 (A) Variation of OCAs and OSAs on the surface after immersing in water with a wide range of pH for about 24 h. **(B)** Underwater crude oil CAs and adhesive forces of the membranes after being kept in water containing 30 $mg \cdot mL^{-1}$ of NaCl, KCl, $CaCl_2$, Na_2SO_4, and $MgSO_4$ for 7 days. **(C)** Long-term stability of the membrane in seawater for 20 weeks. **(D)** Wettability of the surface under the liquid-nitrogen and heating-plate treatment. **(E)** FESEM image of the samples after the test. Variations of CAs and SAs of water and DMF measured on Cotton@HMS@PDMS for treatment in **(F)** high temperature and **(G)** UV irradiation for different time. **(H)** Optical image of continuous vapor condensation on Teflon AF surface and

PIPS surface at different times. **(I)** Contact angles and contact angle hysteresis of CuO nanoblade PIPS remained nearly unchanged after 4800+ h of testing.

Yu et al. [119] covalently grafted vinyl-terminated PDMS (Vi-PDMS) onto a substrate coated with sulfhydryl-modified hollow mesoporous silica (SH-HMS) through a thiol-ene click reaction to prepare a sturdy and self-healing lubricant grafted smooth surface (LGSS). The coating was placed at a high temperature of 60℃ for 14 days **(Figure 15F)** and exposed to UV light for 28 hours **(Figure 15G)**, with only slight changes in contact angle and sliding angle, demonstrating good high-temperature and UV resistance performance.

The chemical stability of hydrophobic coatings during steam condensation is crucial for industrial condensers. For example, Wilke et al. [120] injected hydrophobic polymer (Teflon AF) directly infused into the nanostructure on the surface of the condenser. After 4800 h of testing, the coating continued to exhibit high-quality dropwise condensation, and the CA and contact angle hysteresis remained almost unchanged **(Figures 15H, 15I)**.

The mechanisms of action for diverse antifouling coatings frequently exhibit variations. **Table 1** provides a summary of typical antifouling coatings commonly employed in both marine and medical applications.

(i) Traditional Antifouling: This category involves the utilization of toxic antifouling agents and/or modification of surface characteristics, such as surface wettability, surface energy, and surface roughness, to inhibit the adhesion of proteins, algae, and/or bacteria.

(ii) Antifouling with Degradable Surfaces: These coatings incorporate degradable bonds within their main chains, rendering the polymer surface susceptible to attack by seawater or enzymes in static conditions. This susceptibility results in the degradation of the polymer into small, water-soluble molecules and the subsequent detachment of fouling adhered to the surface.

(iii) Antifouling with Dynamic Surfaces: This category employs chains that are both degradable and hydrolyzable to create a dynamic surface. The dynamic nature enables the release of adhered organic or inorganic substances.

A comprehensive overview of the various types of antifouling coatings, their resistance

capabilities, properties, and applications, is presented in Table 1.

Table 1 Coatings based on different antifouling types and their properties.

Materials	Antifouling Types	Antifouling strategies	Resistant species	Property	Application
Si-HB-PEI [121]	Traditional antifouling (fungicide)	Kills bacteria	Staphylococcus epidermidis	Contact-killing > 99.99%	/
PDMS-TCM [122]	Traditional antifouling (fungicide)	Hydrolysis	Micrococcus luteus	/	/
PDMS oil [123]	Traditional antifouling (lubricants, SLIPS)	Weak adhesion	*E. coli, S. aureus*, blood	Suppressed by >99%	Scalpel
HTS-SLIPS [71]	Traditional antifouling (lubricants, SLIPS)	Weak Adhesion	$CaCO_3$	Ca content was 4.46 wt%	Tube
POEGMA [124]	Traditional antifouling (hydrophilic surface)	Form a hydrated surface	BSA	Fluorescence intensity decreased by 100-fold	Biosensing devices
PVA/PTPM [78]	Traditional antifouling (hydrophilic surface)	Form a hydrated surface	Fog	Antifogging duration for 30 min	Eyeglass
SiO_2 film [77]	Traditional antifouling (hydrophilic surface)	Weak adhesion	Fog	Transmittance was 95% in spray 60 s	/
Silicone oil/liquid paraffin organogel [81]	Traditional antifouling (hydrophilic surface)	Weak Adhesion	Ice	Ice adhesive strength (1 kPa)	
pTMAO/pSB_1/pSB_1 hydrogel [59]	Traditional antifouling (zwitterionic, hydrophilic surface)	Form a hydrated surface	Fibrinogen; undiluted serum, BSA	Decreasing 99.5%	/
pCBM/pSB hydrogel [65]	Traditional antifouling (zwitterionic, hydrophilic surface)	Form a hydrated surface	Blood	Thrombosis weight reduced to 51 ± 18 mg	PVC tubing
Polyacrylamide Hydrogel [62]	Traditional antifouling (zwitterionic, hydrophilic surface)	Form a hydrated surface	Blood	Lowest platelet counts (82.0 ± 15 platelets cm^{-2})	Electrochemical Biosensors
BSA@PSBMA [53]	Traditional antifouling (zwitterionic, hydrophilic surface)	Form a hydrated surface	BSA	Adsorption of 50.3 $ng \cdot cm^{-2}$	Artificial blood vessels

TMAO polymer brush [69]	Traditional antifouling (zwitterionic, hydrophilic surface)	Form a hydrated surface	NaCl	/	/
TiO_2/SiO_2 [52]	Traditional antifouling (amphiphilic surface)	Form a hydrated surface	BSA	Protein adhesion force was 0.39 ± 0.17 nN	Microchip
Superhydrophobic polystyrene surface [61]	Traditional antifouling (hydrophobic surfaces)	Weak adhesion	Blood	>4200× reduction of blood residue area	/
SiO_2/PDMS [125]	Traditional antifouling (hydrophobic surfaces)	Weak adhesion	Blood	/	Tube / blood pump
SiO_2/silicone oil [126]	Traditional antifouling (hydrophobic surfaces)	Weak adhesion	Blood	/	Endoscope
PPS/PTFE [70]	Traditional antifouling (hydrophobic surfaces)	Weak adhesion	$CaCO_3$	Scaling rate of $CaCO_3$ was 0.88 $mg \cdot cm^{-2}$	/
PSiUr [82]	Traditional antifouling (hydrophobic surfaces)	Weak adhesion	Ice	Ice adhesive strength (7 ± 1 kPa)	/
PTCBE elastomer [54]	Traditional Antifouling (SPC)	Hydrolysis	Fibrinogen	Protein adsorption <5%	Tube / catheter
Silicon armor [40]	Traditional antifouling (protective structure)	Weak Adhesion	Water	/	/
CF_4-MP-PVDF [41]	Traditional antifouling (protective structure)	Weak Adhesion	Water	/	/
PCL-PU [43]	Degradable surface	Main chain degradable	bacteria, actinomycetes, and fungi	/	/
P(MMA-CL) Polymer [44]	Degradable surface	Main chain degradable	bacteria, actinomycetes, and fungi	/	/
TCB-TCPM [48]	Dynamic surface	Degradable and Hydrolysis	Pseudomonas sp.	Relative bacterial adsorption <1%	/
PMCMx Polymer [127]	Dynamic surface	Degradable and Hydrolysis	Pseudomonas sp., Vibrio alginolyticus, *E. coli.*	/	/

*Si-HB-PEI, hyperbranched polyurea coatings with polyethyleneimine; PDMS, poly(dimethylsiloxane); TCM,

N-(2,4,6-trichlorophenyl) maleimide; HTS-SLIPS, high-temperature scale-resistant slippery lubricant-induced surface; POEGMA, poly(oligo(ethylene glycol) methyl ether methacrylate; PVA, poly(vinyl alcohol); PTPM, hydrophobic poly 3-(trimethoxysilyl) propyl methacrylate; TMAO, Trimethylamine N-oxide; pSB_1, [2-(Methacryloyloxy)ethyl]dimethyl-(3-sulfopropyl)ammonium hydroxide; pCBM poly(carboxybetaine) microgel; pSB, poly(sulfobetaine); BSA, bovine serum albumin; SBMA, sulfobetaine methacrylate; PPS/PTFE, poly(phenylene sulfide)/polytetrafluoroethylene; PSiUr, poly-silicone-urea. PTCBE, tertiary carboxybetaine ester polymer; CF_4-MP-PVDF: superhydrophobic membrane surface (MP-PVDF) of polyvinylidene difluoride with CF_4 plasma treatment; PCL-PU, PCL diol based polyurethane; PMMA, poly(methylmethacrylate); TCB, tertiary carboxybetaine ester; TCPM, N-(2,4,6-trichlorophenyl)maleimide; PMCMx, polymerization of 2-methylene-1,3-dioxepane (MDO).

4. Application of non-toxic antifouling coatings

4.1 Marine and industrial equipment

4.1.1 Marine Antifouling

Biofouling, also known as fouling, is a naturally-occurring phenomenon characterized by the accumulation, settlement, and rapid colonization of marine organisms such as bacteria, algae, and mollusks on submerged surfaces [128]. These surfaces include ship hulls [129], pipelines [130], oil platforms [131], and ocean sensors [132] found in marine environments. The consequences of biofouling are profound, especially for marine industries, as it leads to surface deterioration, heightened roughness, elevated fuel consumption, and a decrease in vessel speed. At present, diverse antifouling coatings have been widely used in ship hulls, pipelines, oil platforms, and ocean sensors, etc.

A nanocomposite superhydrophobic coating [133] was fabricated using a simple sol-gel synthesis method, utilizing naturally sourced nanomaterials, specifically cellulose nanocrystals (CNCs), as nanofillers. The resulting crosslinked polymer structures exhibited morphologies resembling the curly ridges and grooves found on S. apetala leaves **(Figure 16A)**. Following one week of immersion in a diatom suspension during the exponential growth phase, the coated glass exhibited significantly reduced diatom accumulation compared to bare glass, achieving an over 90% reduction in diatom density **(Figure 16B)**. Furthermore, the incorporation of CNCs at an appropriate concentration enhanced the stability of the coatings. Even after two weeks of immersion in seawater, the coatings maintained their hydrophobicity **(Figures 16C, 16D)**.

Escherichia coli and Staphylococcus aureus, common marine bacteria and pathogens, are key targets for inhibition in antifouling coatings. The nanocomposite superhydrophobic coating [134], synthesized using a simple sol-gel method and incorporating natural nanomaterials (CNCs, **Figure 16E**) as fillers, exhibits exceptional bactericidal activity, achieving nearly 100% efficacy in eradicating Escherichia coli **(Figure 16F)**. Furthermore, after being immersed in seawater for a period of two years, the hybrid coating surface remains free of barnacles and shows reduced accumulation of other contaminants, thus indicating excellent antifouling performance **(Figure 16G)**. Another noteworthy example is the antifouling film developed by Zhang et al. [135], which utilizes three-dimensional BiOI flower-like microspheres **(Figure 16H)**. This film exhibits an impressive antibacterial rate of 99.78% against Staphylococcus aureus **(Figures 16I, 16J)**. Consequently, the versatility of coatings with diverse antifouling properties extends to applications in antibacterial coatings, addressing concerns related to medical infections, including wound dressings and healthcare settings. These aspects will be elaborated on in section 4.2.

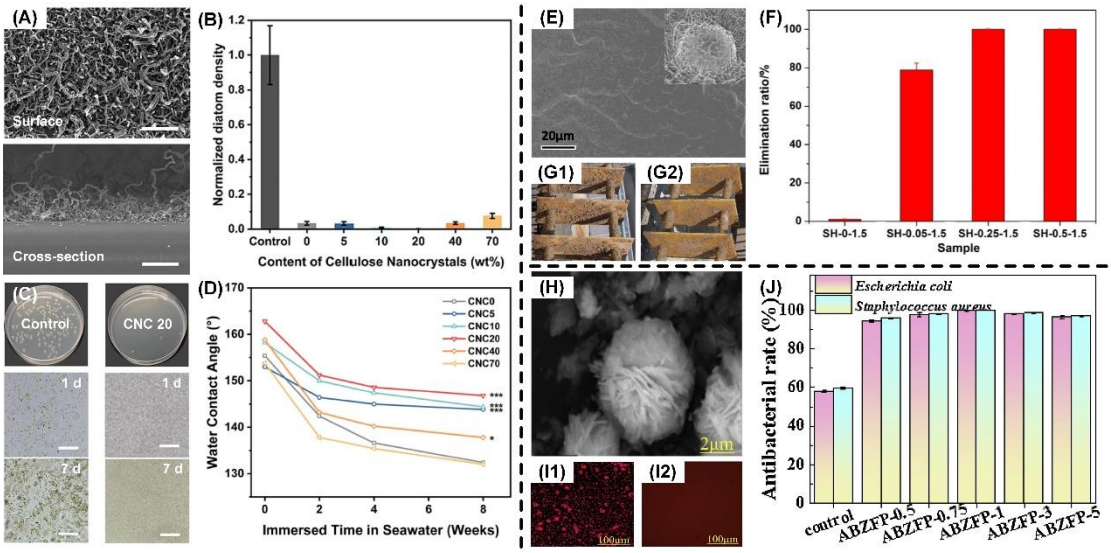

Figure 16 (A) Morphology characterization of CNC20 coatings. Scale bar=5 μm. (B) Statistical chart of diatom density after 7 days' immersion. (C) Antibacterial test: Images of agar plates (top); Anti-diatom test: Microscopy images of diatom adhered on the surface of coatings (middle and bottom). Scale bar=100 μm. (D) Time-dependent variation in WCA in seawater. **(E)** SEM image of the silicone-based SH-0.25-1.5 coating. **(F)** The killing efficiency of the coatings by quantitative evaluation (*E. coli*). The field test results of the EP plate without coating **(G1)** and with SH-0.25-1.5 silicone-based coatings **(G2)** in the South China Sea for 2 years. **(H)** The SEM images of the Bi_5O_7I/Ag flower-like microspheres. Fluorescence

microscope images of the ABZFP films: **(I1)** blank, **(I2)** ABZFP-1 immersed in Nitzschia closterium algae solution after 30 days. **(J)** Antibacterial rates of different ABZFP films for *E. coil* and *S. aureus*.

4.1.2 Marine anti-corrosion

Antifouling coatings **(Figure 17A1)** have been widely employed to reduce biofouling. However, the majority of these coatings exhibit inadequate anti-corrosion performance, resulting in pronounced corrosion of the metal substrate. This often leads to the formation of rust on the substrate surface, which in turn triggers the generation of bubbles between the coating and substrate, ultimately resulting in detachment [136]. Consequently, corrosion remains an unresolved challenge, leading to significant annual economic losses, particularly in the marine industry due to the corrosive environment [137]. To address this issue, rough and porous TO nano-textured films [138] were fabricated using square-waveform, pulsed, cathodic electrodeposition **(Figure 17A2)**. Square wave-pulsed deposition of TO films on stainless steel, as shown in **Figure 17B**, reveals the film thickness and hierarchically structured island morphology. These films exhibit superhydrophobic and liquid-infused surface characteristics, which protect the metal substrate from highly corrosive etchants **(Figures 17C, 17D)**. In addition, Chong et al. [139] successfully encapsulated 8-HQ dissolved in clove oil via an in-situ polymerization technique to create multifunctional microcapsules with antibacterial and anticorrosion properties **(Figure 17E)**. The proposed antibacterial mechanism of the multifunctional coating is depicted in **Figure 17F**, illustrating the release of clove oil from the microcapsules to form a corrosion inhibition layer, thus retarding corrosion attack. To simulate physical damage that may occur in industrial marine applications, a physical scratch was made on the coating, followed by immersion in a 3.5 wt% NaCl aqueous solution at room temperature for 24 hours. Electrochemical corrosion measurements demonstrated that the addition of microcapsules reduced the current density of the coatings **(Figure 17G)**. This reduction was attributed to the rupture of microcapsules at the damaged site, which allowed the released 8-HQ compound to react with iron atoms in the steel matrix, forming a black corrosion inhibitor layer **(Figures 17G1, 17G2)**. This immediate response of the coating inhibited further

corrosion damage. Furthermore, **Figures 17H1-17H4** illustrates the long-term anticorrosion effectiveness of microcapsule-based EP coatings, as black corrosion inhibition layers were formed even after 30 days of immersion in a 3.5 wt% NaCl solution, thus impeding corrosion and safeguarding the underlying substrate. The exceptional corrosion resistance of these coatings suggests their potential as new non-toxic antifouling coatings. Developing non-toxic, environmentally friendly corrosion-resistant coatings offers an effective solution to address steel corrosion in marine environments. This endeavor introduces a fresh perspective and alternative within the domain of marine environmental protection.

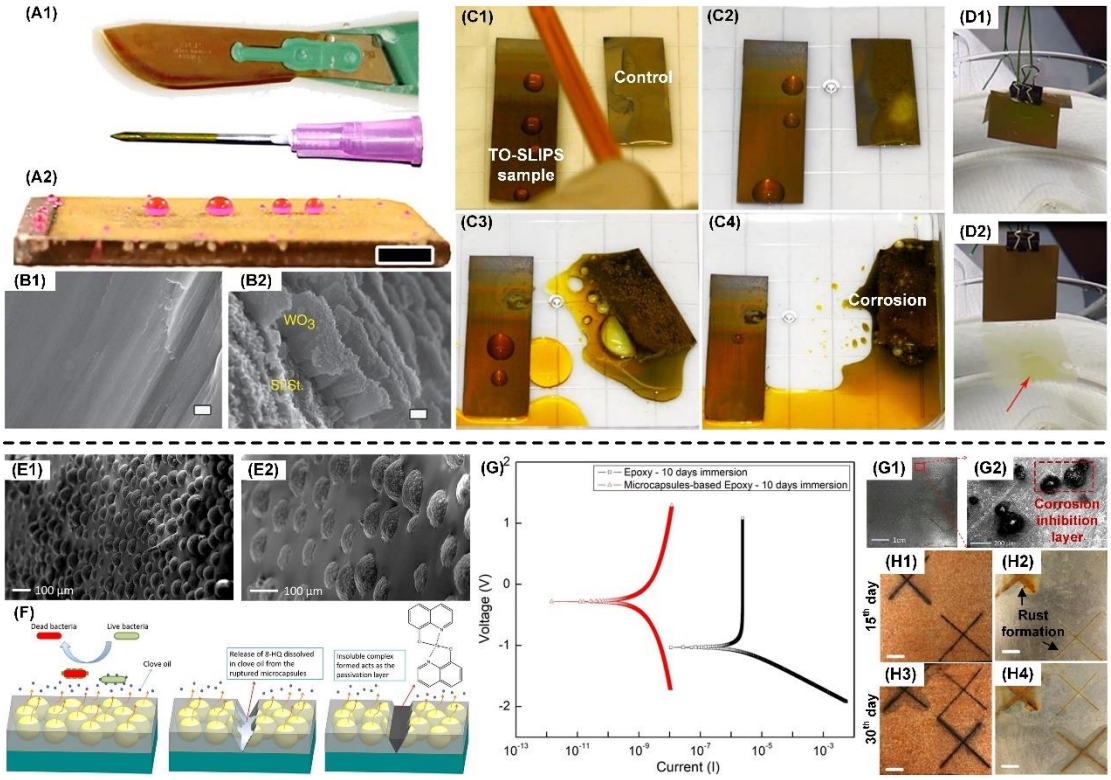

Figure 17 TO films were deposited on several working electrode geometries made from various grades of steel: **(A1)** a surgical-grade steel scalpel blade and syringe needle coated with TO on both internal and external surfaces, and **(A2)** a naval construction HY-100 grade steel plate. Scale bar, 1 cm. **(B1)** SEM image of a bare AISI 304 stainless-steel surface, **(B2)** SEM images of TO films (tilted view, 70°). Scale bar, 200 nm. **(C)** Accelerated corrosion test. **(C1-C4)** Images show corrosion evolution as a function of contact time. **(D1-D2)** Pulling of the TO-SLIPS sample from the media through the air–water interface after being exposed to C. reinhardtii culture for 8 days to grow biofilm. **(E1-E2)** Fabrication of EP with partially embedded microcapsules through controlling the curing time of the EP matrix. **(F)** Mechanism of multifunctional coatings with antibacterial and anticorrosion features. **(G)** Tafel plot for unscratched blank EP coatings and microcapsules-based EP coatings after 10 days of immersion in 3.5 wt% NaCl solution. Optical images of underlying steel substrate for **(G1)**

multifunctional coating containing fabricated microcapsules, in which the SEM images indicates **(G2)** the formation of dark color corrosion inhibition layer as a result of the reaction between the released 8-HQ compound and steel surface. Long-term stability of the fabricated microcapsules in anticorrosion coating **(H1, H3)** allows the effective formation of dark color complexes after multiple scratches of immersion in 3.5 wt% NaCl solution. Rust formation was clearly observed in EP coating **(H2, H4)** after multiple scratches of immersion in 3.5 wt% NaCl solution.

4.1.3 Marine sensors

Marine sensors require long-term resistance to biological adhesion in the marine environment to ensure reliable performance. Biofouling poses a significant challenge due to multiple factors, including the diverse range of fouling species, varied attachment behaviors and adhesion mechanisms, and geographical and seasonal variations [140]. Current antifouling strategies primarily rely on chemical or physical mechanisms, but they often fail to prevent the settlement and attachment of the wide variety of biofouling agents [141]. To address this issue, Zhang et al. [142] developed antifouling surfaces using magnetic artificial cilia (MAC). These active cilia, actuated by a rotating magnet, effectively remove microparticles representing fouling agents or cells from ciliated areas **(Figures 18A1-18A5)**. SEM images confirm the cylindrical shape of the MAC, with a diameter of 50 μm and a height of 350 μm **(Figures 18B1, 18B2)**. **Figures 18C1-18C3** present sequential snapshots from an experiment showing the MAC executing ITC motion at 40 Hz. It is evident that a majority of the particles were successfully removed from the ciliated area within a minute. **Figure 18D** demonstrates that a higher actuation frequency leads to a shorter time required to achieve cleanliness, with 90% cleanness achieved within 10 seconds at a rotation speed of 40 Hz. Additionally, the antifouling coating demonstrates its effectiveness in removing sand particles from the ciliated area **(Figures 18E1-18E3)**.

The antifouling coating used for marine sensors can not only clean the fouling on the equipment surface, but also actively absorb the harmful substance copper in seawater, which can be released as an effective biocide by applying voltage. A porous and cross-linked poly(ethylene imine) structure **(Figure 18F)** was employed in marine and fouling environments to absorb available copper from natural seawater [143]. Electrochemical release of the absorbed

copper at 1.3 V vs Ag/AgCl resulted in a significant reduction of marine growth by 94% compared to the control electrode (coupon) at 0 V **(Figures 18G, 18H1-18H5)**. The antifouling coatings developed for sensors not only offer a reliable method to mitigate biofouling-related sensor accuracy issues but also serve as a noteworthy example of non-toxic antifouling strategies. These findings have the potential to inspire further advancements in the field of marine antifouling. Antifouling coatings applied to ocean sensors play a pivotal role in enhancing their development and sensitivity. Consequently, this facilitates the deployment of wearable devices in underwater environments, advances ocean exploration and monitoring capabilities, and brings the vision of an ocean internet closer to fruition, thereby establishing a robust intelligent system for underwater operations.

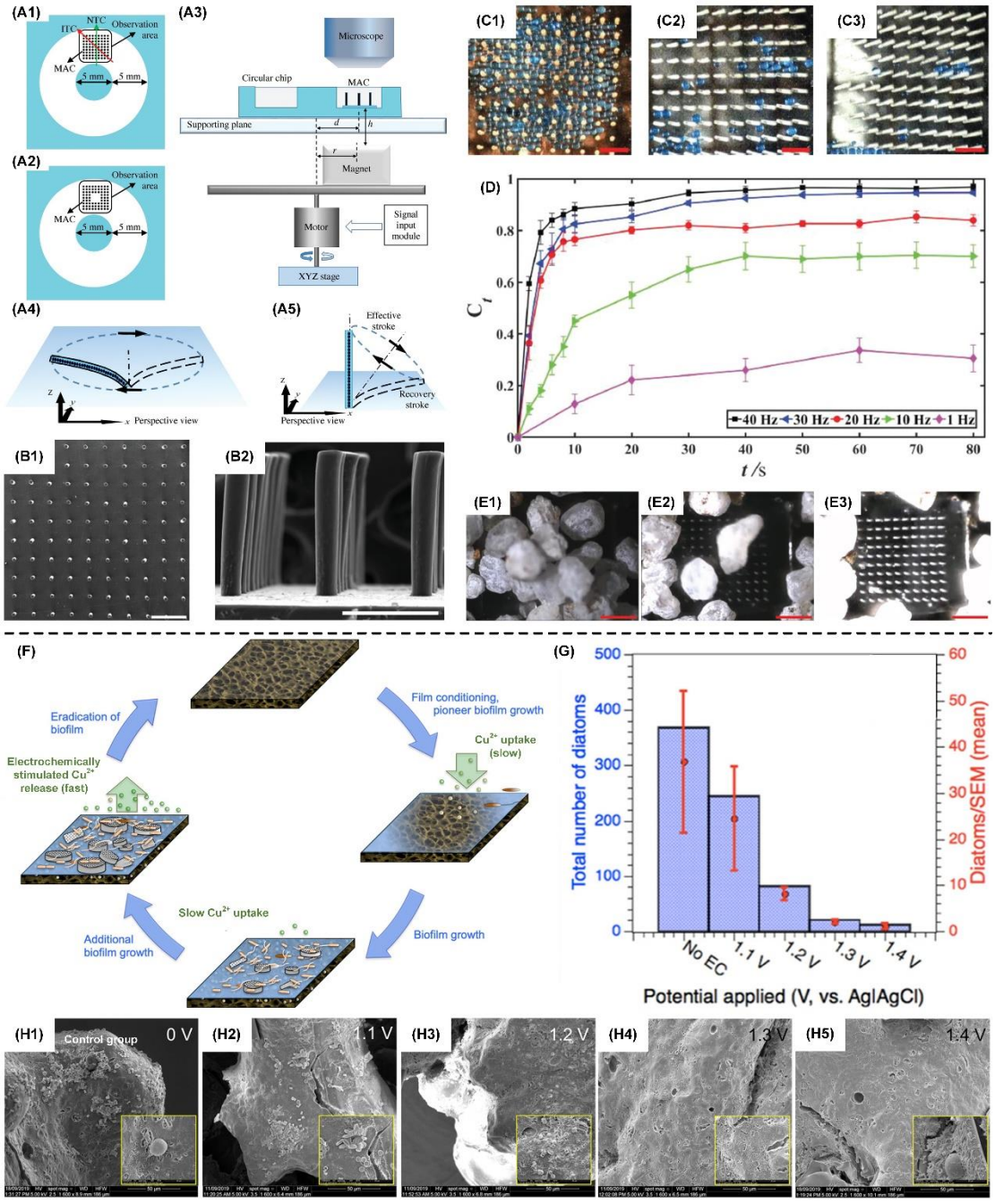

Figure 18 Schematic drawing of the open-top circular chip integrated with **(A1)** a fully ciliated surface and **(A2)** a partially ciliated surface, indicating the location of the ciliated surfaces and the observation area. **(A3-A5)** Actuation scheme of the fabricated MAC. Top-view SEM images of **(B1)** a "fully ciliated surface" covered with orthogonally arranged MAC in a square array of 10 × 10=100 cilia. **(B2)** A side-view SEM image of the MAC, with a diameter, a height, and a pitch of 50, 350, and 250 μm, respectively. The scale bar is 250 μm. **(C1-C3)** Snapshots from one recorded experiment after the MAC operate for **(C1)** 0 s (because the particles have a slightly larger density than water, they are all settled in between the MAC on the PDMS substrate initially), **(C2)** 10 s, and **(C3)** 1 min, showing that particles (blue) are gradually removed from the ciliated area. Scale bars are 500 μm. **(D)** Calculated cleanness as a function of the operating time at different revolution frequencies of the MAC when the MAC perform

the ITC motion. The cleanness is now defined as Ct=(N_0-N_t)/N_0, where N_0 is the number of particles within the ciliated area at time 0, and N_t is the number of particles left after the MAC operating for t seconds. Snapshots from one recorded experiment after the MAC operate for **(E1)** 0 s (because the sand grains have a larger size than the cilia pitch, they all settle on top of the cilia tips initially), **(E2)** 16 s, and **(E3)** 30 s, showing that all sand grains are gradually removed from the ciliated area. **(F)** Working principle of a porous and cross-linked PEI film for the selective uptake of copper ions from natural seawater and electrochemical release at selected time scales to combat marine growth. **(G)** Total number of grown diatom species (blue) counted on all SEM images taken at selected electrode sites and the average number of diatoms per SEM image (red) plotted against their applied potential. Representative SEM images of PEI@CC-NH_2 electrodes (coupons) treated at 0 **(H1)**, 1.1 **(H2)**, 1.2 **(H3)**, 1.3 **(H4)**, and 1.4 V **(H5)** vs Ag/AgCl during marine growth. The insets show selected segments of the grown species on the electrodes at higher magnifications, each.

4.1.4 Oil-water separation

Membrane-based oil/water separation materials, commonly referred to as oil/water separation membranes, have gained significant attention due to their straightforward operation, high separation efficiency, mechanical flexibility, and seamless integration [144]. They find extensive applications in fisheries, mariculture, and marine environments [145]. For instance, a bioinspired bubble-mediated antifouling strategy is employed to fabricate an electrocatalytic porous membrane (CoP/SSM), where hierarchical cobalt phosphide (CoP) arrays are grown on a stainless steel mesh (SSM) [146] **(Figure 19A)**. To assess the oil-water separation capabilities, Nile red-labeled oil drops are subjected to separation tests, revealing the effective performance of Co(OH)F/SSM and CoP/SSM in separating oil-water emulsions **(Figures 19B, 19C)**. After separation using CoP/SSM, the emulsions become clear, and oil droplets within the particle size range of 0.8-10 μm are successfully removed **(Figure 19D)**. In cases where the membrane pores become clogged with oil, the application of a 15 V pressure results in the deformation and outward expansion of the trapped oil droplet, effectively clearing the pore channel within a mere 0.81 seconds **(Figure 19E)**. Furthermore, the membrane exhibits stable and high flux over long-term separation, as evidenced by the continuous generation of microbubbles for 10 minutes under a voltage of -60 V, with only minimal oily sand deposition on the membrane surface **(Figures 19F, 19G)**. The successful development of the oil-water separation membrane not only provides valuable insights but also serves as a basis for the advancement of separation

products for marine and industrial oily wastewater treatment. The development of antifouling separation membrane materials can maintain high separation flux and extend the service life of the membrane layer, which can effectively solve the additional cleaning costs and energy consumption generated in industrial separation.

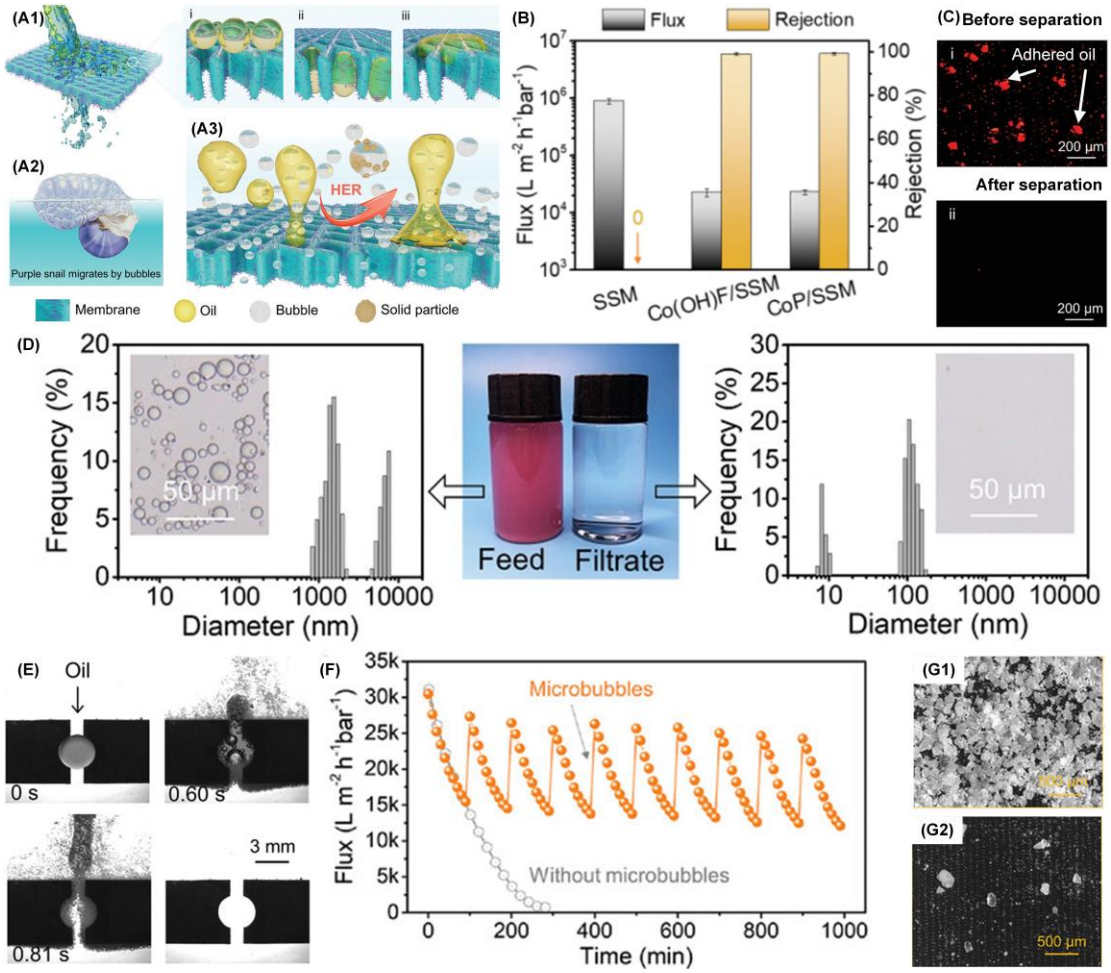

Figure 19 (A1-A3) Bioinspired bubble-mediated dynamic antifouling strategy. **(A1)** The separation of oily wastewater by membrane. Membrane fouling in separating oily wastewater, i) oil stacking on membrane surface, ii) oil blocking in membrane pores, and iii) oil adhering on the membrane surface. **(A2)** The drifting of purple snail by bubbles. **(A3)** Bioinspired dynamic antifouling by bubble-mediated shape morphing.
(B) The average flux and oil rejection of SSM, Co(OH)F/SSM and CoP/SSM in separating oil-water emulsion at 0.1 bar. **(C)** Fluorescence labeling of the adhered oil i) on the used CoP/SSM and ii) after being cleaned by microbubbles. **(D)** Photos and size distribution of emulsified oil before and after being separated by CoP/SSM. **(E)** Removing clogged oil from simulated membrane pores at -15 V. **(F)** Flux variation of CoP/SSM in separating oil-sand-water emulsions. The used CoP/SSM **(G1)** before and **(G2)** after generating microbubbles.

4.2 Surgical equipment in hospitals

4.2.1 Wound dressings

Wound dressings serve as protective barriers that shield wounds from external agents [147, 148]. A crucial requirement for such protective equipment is the eradication of bacteria and prevention of their adherence [149, 150]. To address this need, a functionalized polyurethane (PU) surface (PU-Au-PEG) with inherent antifouling and photothermal bactericidal properties is readily prepared using a NIR-responsive organic/inorganic hybrid coating comprising gold nanorods (Au NRs) and PEG **(Figure 20A)** [151]. The PU-Au-PEG surface demonstrates high bactericidal efficacy before and after NIR irradiation **(Figure 20B)**. Importantly, the dead bacteria can be easily removed, preventing the accumulation of bacterial debris **(Figure 20C)**. Furthermore, after a 3-day period of operation, the surrounding tissues show normal appearance around PU-Au-PEG **(Figure 20D)**. Rodriguez et al. [152] employ a combination of polymer brushes' exceptional performance and the rapid killing effect of endolysins to design an ultra-thin coating for wound dressings. Minimal protein deposits (less than 28 ng cm^{-2}) are observed on these coatings, representing an 89% reduction compared to bare PCL surfaces **(Figure 20E)**. Following a 24-hour incubation in an *E. coli* (DSM-1103) suspension (107 CFU), the coated meshes exhibit minimal presence of bacteria, while the bare fibers are fully covered **(Figure 20F)**. Similarly, the coatings demonstrate an efficient inhibitory effect on *S. agalactiae*, effectively clearing the treated area and eradicating 96% of bacteria **(Figures 20G, 20H)**. Importantly, the coated surfaces remain uncolonized, even in the presence of residue from dead bacteria **(Figure 20I)**. Consequently, the application of antifouling coatings on wound dressings offers an effective means to prevent bacterial infections.

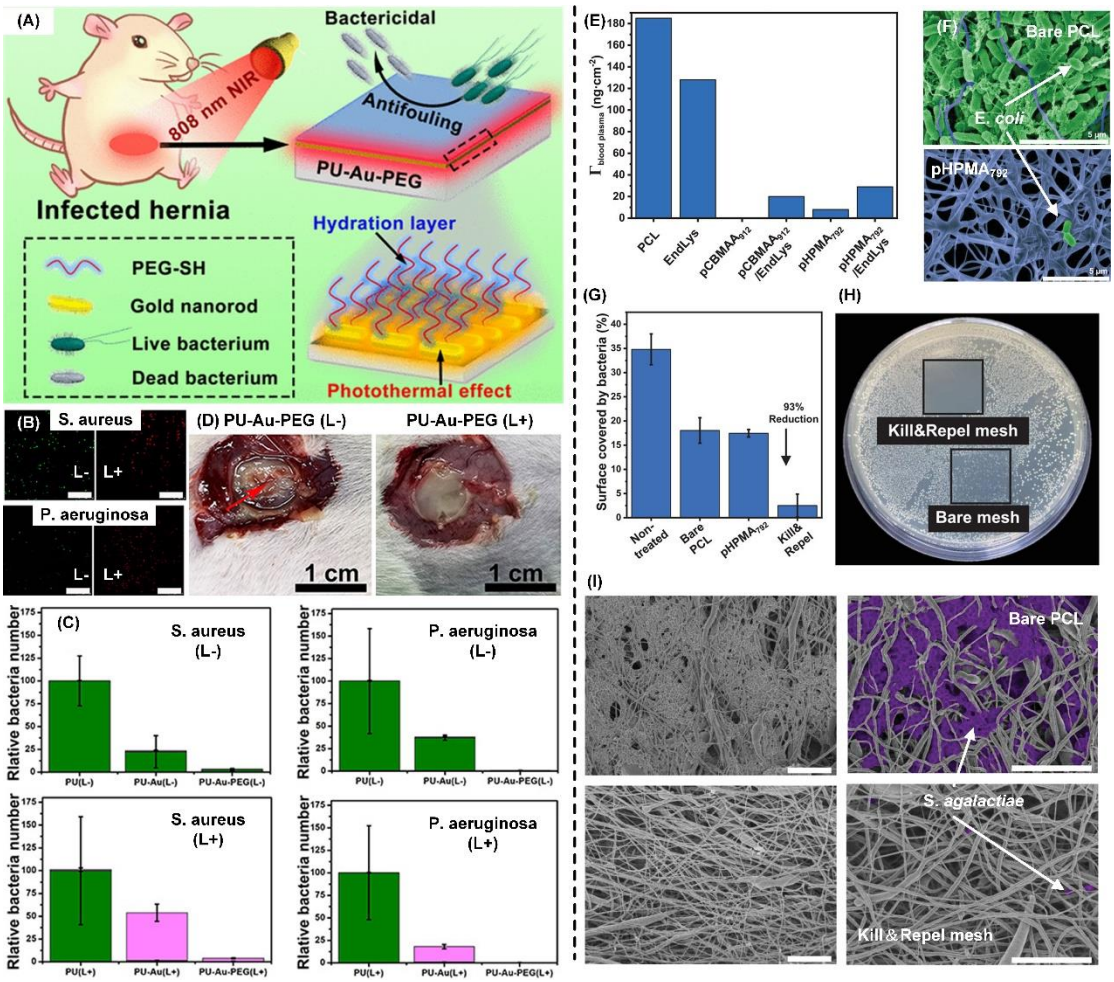

Figure 20 (A) Schematic Illustration of NIR-Responsive PU-Au-PEG Surface with Antifouling and Photothermal Bactericidal Properties. **(B)** Representative CLSM images of *S. aureus* and *P. aeruginosa* on PU, PU-Au, and PU-Au-PEG surfaces without (L-) and with (L+) NIR irradiation (scale bar: 50 µm). **(C)** Relative amounts of *S. aureus* and *P. aeruginosa* adhered on the sample surfaces. Green bars showed the amounts of live bacteria, and pink bars showed dead bacteria. **(D)** General views of infected hernia treatment at 3 d. **(E)** Fouling of blood plasma proteins measured by SPR on bare PCL and PCL coated with LCI-eGFP-Polymers, LCI-EndLys, and mixed coatings at a ratio of 90 to 10 mol%, respectively. **(F)** SEM micrographs of bare and functionalized PCL meshes (LCI-eGFP-HPMA792). **(G)** Agar plate after 24 h of contact: Kill&Repel meshes were able to clear bacterial colonization from the contacted area. **(H)** Quantification of the agar surface covered by *S. agalactiae*. **(I)** SEM images displaying massive adsorption of bacteria on bare meshes. Functionalized meshes did not permit the adhesion of bacteria and bacterial debris. Scale bars are 10 µm.

4.2.2 Biomedical device

Inspection devices often face obstruction caused by highly contaminated fluids, which compromises their visual field and overall functionality [153]. This issue is particularly

pronounced in endoscopes, where the diagnosis and treatment of diseases are hindered by the obscuring of the operative field due to bodily fluids [154]. To address this, Sunny et al. [126] employed a LBL deposition protocol using 20-nm silica particles and poly(diallyldimethylammonium chloride) to create a mechanically robust, porous silica network measuring 100-nm in thickness on glass surfaces. The feature sizes and porosity of this silica network impart antireflective properties to the material, enhancing its transparency when infused with a liquid compared to the underlying plain glass. **(Figure 21A)**. With the bronchoscope coated with the liquid-infused material that maintains a clear vision during biopsy, allowing rapid recovery within 4 s even if vision loss occurs **(Figure 21B)**.

Tesler et al. [123] demonstrated a method for creating hydrophobic and lubricant-infused slippery surfaces by grafting bare PDMS oil onto non-photoactive solid substrates **(Figure 21C)**. Through UV light exposure, PDMS oil dissociates without requiring a photocatalyst and then grafts onto virtually any surface. The coated surfaces exhibit excellent corrosion protection for metals, repel complex liquids such as blood. MSS blades grafted with PDMS oil displayed a corrosion inhibition efficiency of 98.8%, whereas MSS blades (grafted and infused) not only exhibited lower corrosion potential but also demonstrated a reduced current density in the passive region, resulting in a noisy signal of 10^{-9} A·cm^{-2} **(Figure 21D)**. When the medical device comes into contact with blood, which may lead to the formation of thrombosis, the amount of blood attached to the UV-Vis transplant scalpel and PDMS perfusion scalpel is significantly reduced after soaking in a petri dish containing fresh blood **(Figures 21E, 21F)**. This superior blood repellent performance can be attributed to the presence of a stable liquid–liquid interface formed between the low-surface-tension liquid and blood, contrasting with the easily contaminated solid surface of bare scalpels.

Li et al. [125] introduced a novel sand-casting technique for fabricating a superhydrophobic and blood-repelling surface composed of silicone and functionalized SiO_2 NPs. The blood contact angle of the resulting sample was measured to be 150.6° ± 1.44° **(Figure 21G)**, and the demonstrated liquid and blood repellence properties of the sand-casted SHP material could potentially mitigate shear forces experienced by blood, thus reducing blood

damage. Moreover, this technique can be employed to cast SHP housings for centrifugal blood pumps, such as the Affinity™ CP blood pump **(Figure 21H)**. The satisfactory performance of these antifouling coatings has expedited the advancement of biomedical devices and holds great potential for application in clinical fields.

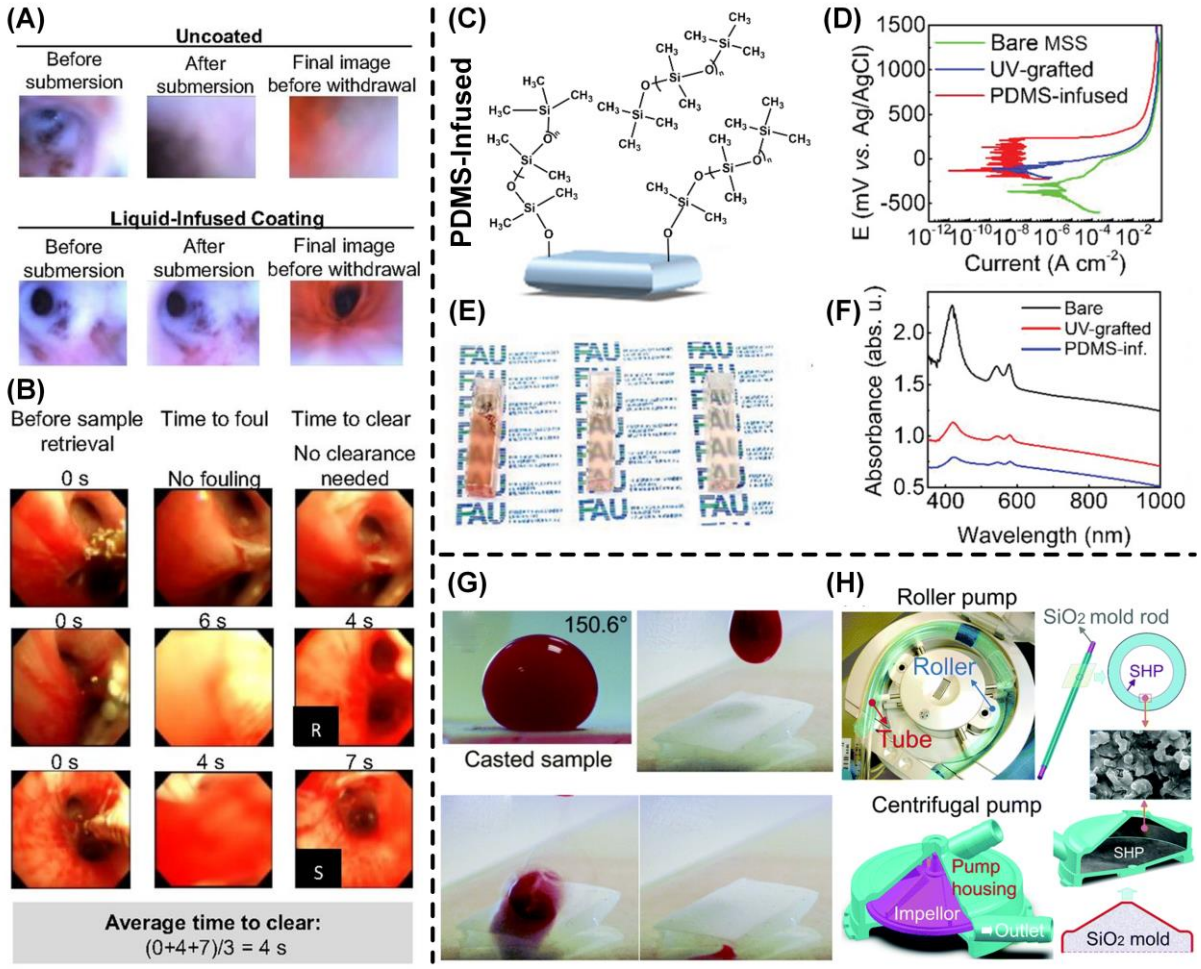

Figure 21 (A) The examination procedures of uncoated and coated endoscopes with lung secretions in an ex vivo lung. **(B)** Endobronchial biopsies using a liquid-infused coated bronchoscope are performed in the right lung of a pig. **(C)** Schematic diagram of a smooth surface grafting procedure to form PDMS-infused slippery surfaces. **(D)** Potential dynamic polarization of medical scalpel blade steel in 3.5 wt% NaCl electrolyte of bare, PDMS UV-grafted, and PDMS-infused made of MSS. Optical images **(E)** and UV Vis absorption spectra **(F)** of blood adhered to the surface of the MSS after washing with PBS. **(G)** Illustration of fabricating a 3D SHP centrifugal pump housing, and a roller blood pump tube based on the developed sand-casting method. **(H)** Blood contact angle of the casted SHP sample, blood rolling off the casted sample without leaving stains.

4.2.3 Healthcare

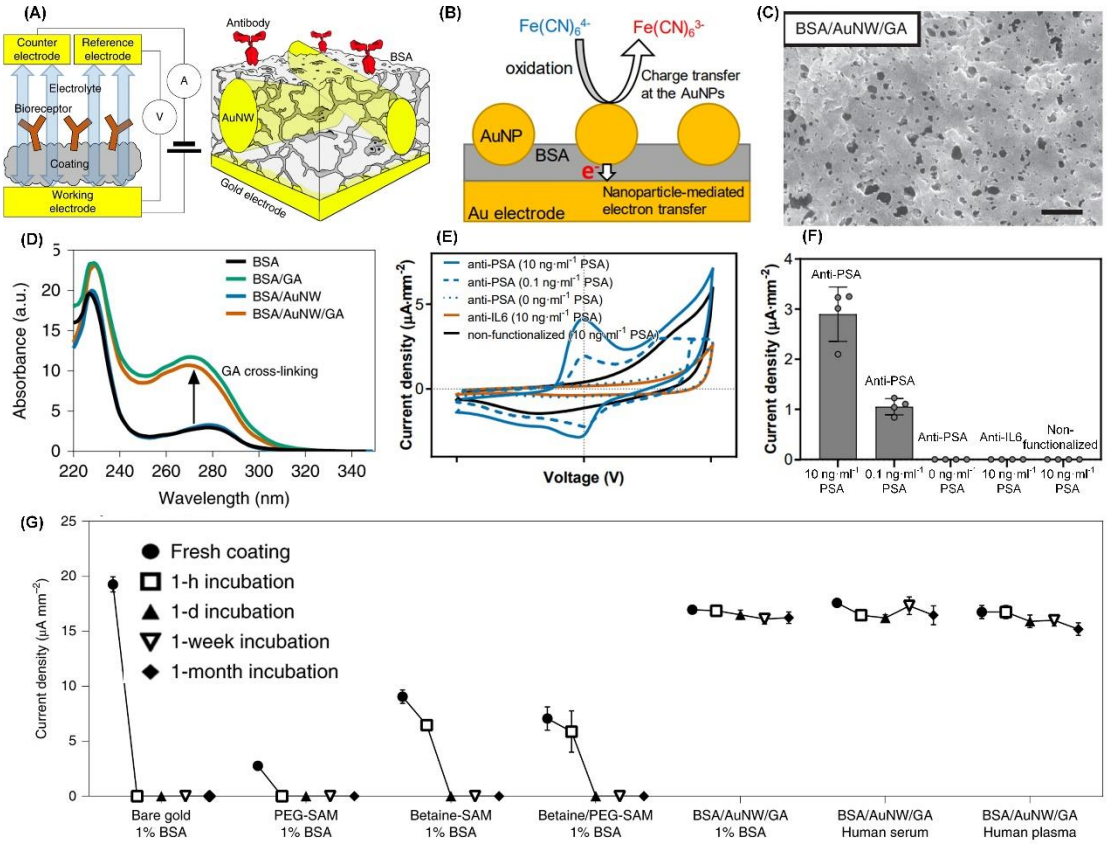

Figure 22 (A) Schematic of the three-electrode electrochemical set-up used (left). Schematic of the BSA/AuNW/GA coating functionalized with antibodies on a gold electrode (right). **(B)** Charge transfer of electroactive diffussible species and electronic communication at BSA/AuNP coated electrodes. **(C)** Scanning electron micrograph of the coated electrodes (scale bar, 400 nm). **(D)** UV absorption spectra of BSA with/without GA and/or AuNW. **(E)** Voltammograms corresponding to the redox of precipitated TMB on BSA/AuNW/GA coated electrodes functionalized with different antibodies. **(F)** Extracted mean value of the current densities from the voltammograms corresponding to the oxidation of precipitated TMB. **(G)** Comparison of mean value of current densities recorded at bare gold electrodes, PEG-SAM-modified electrodes, betaine-SAM-, betaine/PEG-SAM and optimized BSA/AuNW/GA-coated electrodes stored for >30 d at 4°C in 1% BSA, human serum or human plasma.

Affinity-based electrochemical detection in complex biological fluids has the potential to enable multiplexed point-of-care diagnostics for home healthcare [155]. However, traditional antifouling coatings, such as BSA and PEG self-assembled monolayers (PEG-SAMs), impede electron transfer, creating a dilemma for antifouling strategies. From a materials standpoint, Au NPs or CNTs show promise as next-generation antifouling coatings in electrochemical sensors due to their electrical conductivity, functionalization capabilities, and biocompatibility. For instance, Sabaté del Río et al. [156] developed a three-dimensional (3D) nanocomposite

matrix comprising BSA intertwined with conductive nanomaterials like gold nanowires (AuNWs), gold NPs (AuNPs), or CNTs, as depicted in **Figures 22A, 22B**. The porous BSA backbone of the matrix hinders nonspecific protein adsorption while allowing efficient diffusion of soluble electro-active species to the electrode, minimizing hindrance compared to conventional antifouling coatings **(Figure 22C)**. The use of Glutaraldehyde (GA) for crosslinking BSA molecules enhances the overall electrochemical performance of the coating **(Figure 22D)**. To assess the potential adsorption of small, positively charged proteins in plasma onto the coating via electrostatic attraction, leading to pore clogging, an electrochemical enzymatic sandwich detection assay was conducted. a redox current was observed for the positive control, but no signal was detected for the unfunctionalized BSA/AuNW/GA-coated electrode or the electrode functionalized with anti-IL-6 antibody **(Figures 22E, 22F)**. This suggests that electrostatic interactions between positively charged proteins and the BSA coating are not sufficiently strong to cause fouling or pore clogging. Moreover, the BSA/AuNW/GA coating exhibited excellent antifouling performance, with only minimal (~7%) sensitivity loss after exposure to 1% BSA, unprocessed human serum, or plasma for one month **(Figure 22G)**. And these biosensors can be reused with minimal signal loss after washing, enabling repeated measurements for continuous biomarker monitoring.

4.2.4 Droplet manipulation

Droplet manipulation is of great significance in microfluidic, biological analysis, and microreactor equipment [157]. At present, researchers have developed many wetting surfaces to manipulate droplets and introduced external stimuli (such as light, electric field, magnetic field, etc.) to further achieve droplet manipulation [158]. Slippery lubricant-infused porous surface (SLIPS) has low hysteresis and non-stick properties for various liquids, making it a representative of droplet manipulation.

Manabe et al. [159] constructed a photo-responsive liquid transport surface. The coating consists of a long chain alkyl silane that maintains the fluid stability of the lubrication fluid and molecules with azobenzene derivatives (photoresponsive) **(Figure 23A)**. The photoresponsive

molecules acted as light-responsive molecular motor, leading to the isomerization gradient of the flow, and realizing light driven liquid transport. By fixing the irradiation angle and only changing the position of the applied light, the phenomenon of "round-trip" transmission is achieved. When light is applied from one side to pass through the water droplet, the droplet moves relatively slowly at a speed of 0.11 $mm \cdot s^{-1}$. However, when droplets propagate forward relative to the irradiation direction, they move faster at a speed of 0.27 $mm \cdot s^{-1}$ **(Figure 23B)**. Accurate position transmission can be achieved repeatedly by changing the irradiation direction.

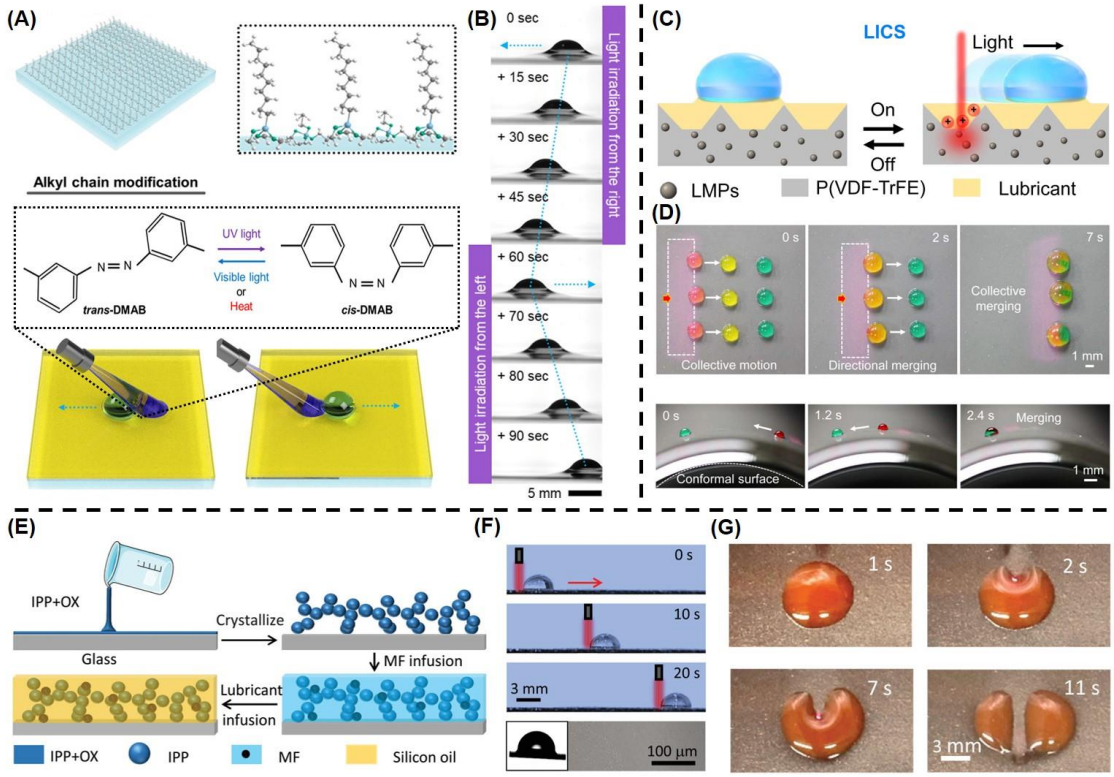

Figure 23 (A) Schematic diagram of strategies for preparing photo driven liquid transport through successive alkyl chain modification and photo responsive liquid layer. **(B)** Images showing the motion of the water droplet by light irradiation. **(C)** Schematic illustration of LICS for droplet manipulation. **(D)** The optical picture of the collective motion and directional merging of water droplets and water droplets moving on a curved smooth surface under NIR radiation. **(E)** Schematic diagram for the preparation of lubricating self-mediating photothermal smooth surface. **(F)** Droplet motion on LSPSS under NIR light irradiation. **(G)** Image of ethanol droplets splitting on LSPSS.

Wang et al. [160] used the dual advantages of solid and lubricant to build a photothermal response composite surface with real-time light-induced surface charge regeneration. The light-

induced charged slippery surface (LICS) consists of microsized Ga-In liquid metal particles (LMPs) used to effectively convert absorbed light into local heat, poly(vinylidene fluoride-co-trifluoroethylene) [P(VDF-TrFE)] copolymer, and a microstructure coated with a layer of hydrophobized SiO_2 NPs **(Figure 23C)**. As shown in **Figure 23D**, three 2 μL droplets can be driven under the control of a single laser beam and then gradually merged with the second and third row droplets. The LICS platform had high flexibility and can fit onto curved substrates for droplet operations, including transportation and merging.

Zhan et al. [161] constructed a lubricant self-mediating photothermal sliding surface (LSPSS) by injecting magnetic fluid (MF) containing Fe_3O_4 and silicone oil into superhydrophobic surfaces with interconnected porous structures **(Figure 23E)**. And by controlling the irradiation route, droplets with low surface tension can not only be driven in the desired direction, but also split proportionally on LSPSS **(Figure 23F)**. **Figure 23G** showed the 10 μL ethanol droplet on the LSPSS that can completely divide the droplet for a short time by moving the point of irradiation. It is of great significance to achieve lossless and efficient transportation in fields such as biomedical diagnostic analysis and microreactor equipment.

5. Conclusions and outlook

The reviewed studies collectively underscore the urgent need for non-toxic alternatives to traditional antifouling coatings. Various traditional strategies have been explored, such as surface modification with different wettability, surface modification with biomimetic textures, incorporation of natural repellents, utilization of environmentally benign compounds, and degradable dynamic antifouling surfaces.

(a) Traditional antifouling coatings, relying on surface wettability as a foundation, encompass FRC, zwitterionic, and (super)hydrophilic/(super)hydrophobic surface coatings, whether or not they incorporate microstructure or cross-linking network protection. These coatings are inherently influenced by surface energy and morphology. In practice, they frequently necessitate the application of external forces, specifically additional shear force, to efficiently dislodge fouling adhering to the surface.

(b) Biodegradable antifouling coatings can decompose their main chains through microbial or chemical means, yielding small molecules. However, reconciling degradation potential with mechanical properties is challenging, and the scarcity of functional cyclic monomers limits their applicability.

(c) Antifouling coatings featuring degradable main chains and hydrolyzable side chains are synthesized through the process of ring-opening polymerization, involving vinyl polymers and cyclic monomers. Precise control of polymer degradation rates is achieved by modifying their structures, leading to exceptional antifouling performance, even in stagnant water environments. However, this category of antifouling coating is constrained by the inherent strength of the polymer, posing challenges for ensuring long-term durability.

As discussed in Sections 3 and 4, most of these strategies have shown excellent results in addressing fouling issues, demonstrating the feasibility of reducing fouling without resorting to toxic agents. Unfortunately, so far, there is no specific strategy that can balance pollution prevention, non-toxic, powerful mechanical properties, and electrochemical corrosion prevention for long-term application in complex marine, medical, and other environments, such as antifouling performance in static environments or at different temperatures/pH. Therefore, urgent need and challenge to create a more robust antifouling film to achieve long-lasting non-toxic antifouling methods by combining multiple antifouling strategies.

In summary, the progression and integration of non-toxic marine antifouling coatings represent a promising approach for mitigating the ecological and health concerns linked to conventional toxic solutions. Nevertheless, substantial efforts remain essential to cultivate enduring and eco-friendly solutions for biological pollution control. This exceptionally fertile field also offers a glimpse into future opportunities.

(I) At present, from the perspective of antifouling durability and antifouling performance, surfaces with biomimetic protective structures and dynamic surfaces composed of polymers with degradable main chain and hydrolyzable side groups have shown promising results. Unfortunately, some non-toxic coatings exhibit short-term antifouling performance comparable to traditional toxic coatings, but their effectiveness under long-term and various

environmental conditions requires further research and testing of the cost-effectiveness, durability, and stability of such physical and chemical combined coatings under seawater. In addition, with the discovery of more bio-friendly natural antifouling agents and synthetic antifouling agents derived from nature in recent years, combining biomimetic structured surfaces with bio-friendly antifouling agents or dynamic surfaces may be a future development trend. However, the high cost and limited manufacturing scale of such methods should be addressed.

(II) Antifouling coatings must exhibit resilience against fluctuations in temperature, salinity, and pH within the application environment, a critical requirement for both marine and medical applications. Traditional zwitterionic coatings, for instance, display inadequate salt resistance, with salt molecules significantly diminishing surface hydration in typical zwitterionic polymers. This disruption to hydration layer formation ultimately compromises the antifouling efficacy of the coating. Hence, it is imperative to meticulously engineer the structure and composition of polymers, minimizing the distance (dipole) between positively and negatively charged groups, to enhance the salt resistance of zwitterionic coatings.

(III) The introduction of intelligent response materials in the coating as Marine antifouling coatings has attracted more and more attention, because they can change the interface characteristics according to small external changes such as temperature, light, pH and salinity, further improving the selectivity of polluting organisms. However, currently most intelligent switchable antifouling surfaces are only used in laboratories, and in the face of complex marine/medical environments, there are still certain difficulties in achieving fast, sensitive, and on-demand control of the release of antifouling materials. In the actual application environment of ship antifouling, it is necessary to choose appropriate stimulation conditions and reasonable preparation processes.

Developing antifouling coatings is crucial to protect marine equipment and prevent infectious diseases. Antifouling technology based on microstructures and dynamic surfaces holds great promise for future environmentally friendly antifouling solutions. The development and adoption of non-toxic marine/medical antifouling coatings represent a promising avenue

for addressing the ecological and health concerns associated with traditional toxic solutions. With further research, innovation, and collaboration, these coatings could usher in a new era of environmentally responsible fouling prevention in marine/medical industries.

CRediT authorship contribution statement

Xuerui Zang: Investigation, Writing - Original Draft, Data Curation. **Yimeng Ni:** Investigation, Visualization. **Qiuyan Wang:** Investigation. **Yan Cheng:** Formal analysis. **Jianying Huang:** Resources. **Xuewen Cao:** Supervision. **Claire J. Carmalt:** Conceptualization. **Yuekun Lai:** Conceptualization. **Dong Ha Kim**: Conceptualization. **Yijiang Liu**: Conceptualization, Writing - Review. **Zhiqun Lin:** Conceptualization, Supervision, Writing - Review & Editing.

Declaration of competing interest

The authors declare that they have no known competing financial interests or personal relationships that could have appeared to influence the work reported in this paper.

Acknowledgments

This work was supported by NUS startup grant, the National Natural Science Foundation of China (52173207), the Science Fund for Distinguished Young Scholars of Hunan Province of China (2023JJ10040), and National Research Foundation of Korea Grant funded by the Korean Government (NRF-2020R 1A 2C 3003958).

Data availability

No data was used for the research described in the article.

References

[1] S. Amini, et al., *Science*, 357 (2017) 668.
[2] M. Fore, *ACS Cent. Sci.*, 6 (2020) 1644.
[3] H. Qiu, et al., *Prog. Polym. Sci*, 127 (2022) 101516.
[4] A. Farhadian, et al., *Chem. Eng. J.*, 431 (2022) 134098.
[5] J. J. Gooding, *Nat. Nanotechnol.*, 14 (2019) 1089.
[6] M. Dai, et al., *JACC-Clin. Electrophy.*, 5 (2019) 1071.
[7] M. Topaz, et al., *J. Am. Coll. Cardiol.*, 81 (2023) 119.
[8] S. M. A. Mousavi, and R. Pitchumani, *Chem. Eng. J.*, 431 (2022) 133960.
[9] S. Guo, et al., *Trends Microbiol.*, 27 (2019) 453.
[10] T. Egghe, et al., *Trends Biotechnol.*, 41 (2023) 63.
[11] M. Lejars, et al., *Chem. Rev.*, 112 (2012) 4347.
[12] H. Guo, et al., *Chem. Eng. J.*, 420 (2021) 127676.
[13] S. Bi, et al., *J. Mater. Sci. Technol.*, 159 (2023) 125.
[14] J. Sha, et al., *Carbon*, 201 (2023) 1038.
[15] D. Wang, et al., *J. Colloid Interface Sci.*, 563 (2020) 261.
[16] J. Tian, et al., *J. Mater. Sci. Technol.*, 79 (2021) 62.
[17] R. Chen, et al., *Adv. Funct. Mater.*, 31 (2021) 2011145.
[18] B. B. Berking, et al., *Angew. Chem. Int. Ed.*, n/a (2023) e202308971.
[19] Y. Zhu, et al., *Adv. Funct. Mater.*, 28 (2018) 1804121.
[20] S. Cao, et al., *Sci. Bull.*, 56 (2011) 598.
[21] P. J. Molino, et al., *ACS Nano*, 12 (2018) 11610.
[22] J. Wellens, et al., *Biosens. Bioelectron.*, 226 (2023) 115121.
[23] Y. Deng, et al., *Compos. B. Eng.*, 225 (2021).
[24] Y. Zhang, et al., *Adv. Sci.*, 9 (2022) 2200268.
[25] G. Fang, et al., *Nano Today*, 48 (2023) 101755.
[26] Y. Xia, et al., *Angew. Chem. Int. Ed.*, 58 (2019) 1308.
[27] J. Sha, et al., *J. Colloid Interface Sci.*, 637 (2023) 67.
[28] W. Li, et al., *Chem. Eng. J.*, 454 (2023) 140057.
[29] K. Xing, et al., *Chem. Eng. J.*, 418 (2021) 129079.
[30] H. Fan, and Z. Guo, *J. Colloid Interface Sci.*, 591 (2021) 418.
[31] J. Yoon, et al., *Adv. Mater.*, 32 (2020) 2002710.
[32] V. Vercillo, et al., *Adv. Funct. Mater.*, 30 (2020) 1910268.
[33] L. Zhang, et al., *Chem. Eng. J.*, 446 (2022) 137461.
[34] Z. Wang, et al., *Small*, 12 (2016) 3827.
[35] Y. Zhao, et al., *Nat. Commun.*, 14 (2023) 2679.
[36] T.-L. Chen, et al., *Adv. Funct. Mater.*, 31 (2021) 2104173.
[37] X. Zhang, et al., *Int. J. Mach. Tool. Manu.*, 185 (2023) 103993.
[38] N. Abu Jarad, et al., *Small*, 19 (2023) 2205761.
[39] X. Zang, et al., *Adv. Sci.*, n/a (2024) 2305839.
[40] D. Wang, et al., *Nature*, 582 (2020) 55.
[41] Z. Xiao, et al., *Desalination*, 466 (2019) 36.

[42] J. Pan, et al., *Acc. Chem. Res.*, 55 (2022) 1586.
[43] C. Ma, et al., *ACS Sustain. Chem. Eng.*, 5 (2017) 6304.
[44] H. Yang, et al., *ACS Appl. Mater. Interfaces*, 12 (2020) 16849.
[45] G. Dai, et al., *ACS Appl. Mater. Interfaces*, 11 (2019) 11947.
[46] D. Aoki, et al., *J. Am. Chem. Soc.*, 139 (2017) 6791.
[47] A. Tardy, et al., *Chem. Rev.*, 117 (2017) 1319.
[48] G. Dai, et al., *ACS Appl. Mater. Interfaces*, 13 (2021) 13735.
[49] W. Xu, et al., *ACS Appl. Mater. Interfaces*, 6 (2014) 4017.
[50] J. Zhang, et al., *ACS Appl. Mater. Interfaces*, 14 (2022) 56097.
[51] M. Beyer, et al., *Biomaterials*, 27 (2006) 3505.
[52] N. Li, et al., *Adv. Mater.*, 33 (2021) 2003559.
[53] Z. Zhao, et al., *Adv. Mater.*, 35 (2023) 2208824.
[54] H.-C. Hung, et al., *Adv. Mater.*, 29 (2017) 1700617.
[55] V. Carniello, et al., *Adv. Colloid Interfac.*, 261 (2018) 1.
[56] H. Ko, et al., *Sci. Adv.*, 5 (2023) eaax8935.
[57] H. Gao, et al., *Adv. Funct. Mater.*, 31 (2021) 2007664.
[58] S. Aleid, et al., *ACS Mater. Lett.*, 4 (2022) 511.
[59] X. Li, et al., *Adv. Mater.*, 33 (2021) 2102479.
[60] K. Stark, and S. Massberg, *Nat. Rev. Cardiol.*, 18 (2021) 666.
[61] J. M. Nokes, et al., *Adv. Healthc. Mater.*, 5 (2016) 593.
[62] D. Chan, et al., *Adv. Mater.*, 34 (2022) 2109764.
[63] Q. Li, et al., *Chem. Rev.*, 122 (2022) 17073.
[64] X. Wang, et al., *Compos. B. Eng.*, 244 (2022) 110164.
[65] M. Yao, et al., *Nat. Commun.*, 13 (2022) 5339.
[66] S. Li, et al., *Chem. Eng. J.*, 431 (2022) 133945.
[67] R. Zang, et al., *Mater. Horiz.*, 9 (2022) 2872.
[68] Y. Zhao, et al., *Adv. Funct. Mater.*, 27 (2017) 1701466.
[69] H. Huang, et al., *J. Am. Chem. Soc.*, 143 (2021) 16786.
[70] H. Qian, et al., *Ind. Eng. Chem. Res.*, 56 (2017) 12663.
[71] X. Yao, et al., *Small*, 18 (2022) 2203615.
[72] N. Horiuchi, *Nat. Photonics*, 17 (2023) 136.
[73] J. Song, et al., *Adv. Compos. Hybrid Ma.*, 6 (2022) 22.
[74] S. Pan, et al., *J. Am. Chem. Soc.*, 143 (2021) 9972.
[75] J. Yoon, et al., *Adv. Mater.*, 32 (2020) 2070256.
[76] H. Guo, et al., *Chem. Eng. J.*, 351 (2018) 409.
[77] Z. Han, et al., *ACS Nano*, 10 (2016) 8591.
[78] J. Shi, et al., *Adv. Sci.*, 9 (2022) 2200072.
[79] W. Wang, et al., *J. Mater. Chem. A*, 11 (2023) 18679.
[80] T. Li, et al., *Appl. Mater. Today*, 26 (2022) 101367.
[81] Y. Ru, et al., *Angew. Chem. Int. Ed.*, 59 (2020) 11876.
[82] J. Chen, et al., *Small*, 18 (2022) 2200532.
[83] P. Hu, et al., *Chem. Eng. J.*, 449 (2022) 137875.

[84] X. Peng, et al., *Adv. Sci.*, 9 (2022) 2203890.
[85] H. Kim, et al., *Adv. Funct. Mater.*, 32 (2022) 2113253.
[86] Y. Li, et al., *Chem. Eng. J.*, 338 (2018) 440.
[87] Z. Tong, et al., *Adv. Funct. Mater.*, 32 (2022) 2201290.
[88] H. Qian, et al., *J. Mater. Chem. A*, 5 (2017) 2355.
[89] Z. Zheng, et al., *Compos. B. Eng.*, 247 (2022) 110321.
[90] P. Hu, et al., *Chem. Eng. J.*, 406 (2021) 126870.
[91] J. Chen, et al., *J. Mater. Chem. A*, 7 (2019) 15207.
[92] M. Liu, et al., *Sci. Adv.*, 5 (2023) eaaw5643.
[93] H. Kuroki, et al., *Adv. Funct. Mater.*, 23 (2013) 4593.
[94] D. Chen, et al., *Adv. Mater.*, 27 (2015) 5882.
[95] G. Wu, et al., *Adv. Funct. Mater.*, 24 (2014) 6751.
[96] N. Guo, et al., *J. Mater. Sci. Technol.*, 66 (2021) 82.
[97] T. Liu, et al., *ACS Appl. Mater. Interfaces*, 10 (2018) 40317.
[98] Y. Ye, et al., *J. Hazard. Mater.*, 364 (2019) 244.
[99] Y. Zou, et al., *Chem. Eng. J.*, 362 (2019) 638.
[100] Z.-Q. Zhang, et al., *J. Magnes. Alloy.*, 9 (2021) 1443.
[101] X. Zang, et al., *Chem. Eng. J.*, 451 (2023) 138573.
[102] W. Zheng, et al., *Adv. Mater.*, 34 (2022) 2204581.
[103] X. Zhao, et al., *Chem. Eng. J.*, 442 (2022) 136017.
[104] Z. Wang, et al., *Chem. Eng. J.*, 408 (2021) 127263.
[105] L.-P. Xu, et al., *ACS Nano*, 7 (2013) 5077.
[106] Y. Qing, et al., *Compos. B. Eng.*, 236 (2022) 109797.
[107] W. Peng, et al., *Chem. Eng. J.*, 352 (2018) 774.
[108] Z. Yu, et al., *Adv. Funct. Mater.*, n/a (2023) 2305995.
[109] W. Tian, et al., *Chem. Eng. J.*, 462 (2023) 142346.
[110] W. Deng, et al., *J. Colloid Interface Sci.*, 642 (2023) 255.
[111] J. Zhang, et al., *Langmuir*, 37 (2021) 6042.
[112] Z. Dai, et al., *Adv. Funct. Mater.*, 31 (2021) 2008574.
[113] M. Liu, et al., *J. Mater. Chem. A*, 5 (2017) 19297.
[114] Y. Li, et al., *J. Mater. Chem. A*, 7 (2019) 7242.
[115] J. E. Gittens, et al., *Biotechnol. Adv.*, 31 (2013) 1738.
[116] C. Li, et al., *Chem. Eng. J.*, 385 (2020) 123924.
[117] S. Zhang, et al., *ACS Nano*, 12 (2018) 795.
[118] D. Li, et al., *Nanoscale*, 13 (2021) 7810.
[119] M. Yu, et al., *J. Colloid Interface Sci.*, 586 (2021) 279.
[120] K. L. Wilke, et al., *ACS Nano*, 14 (2020) 14878.
[121] L. A. T. W. Asri, et al., *Adv. Funct. Mater.*, 24 (2014) 346.
[122] Q. Xie, et al., *ACS Appl. Mater. Interfaces*, 7 (2015) 21030.
[123] A. B. Tesler, et al., *Adv. Funct. Mater.*, 31 (2021) 2101090.
[124] D. Y. Joh, et al., *ACS Appl. Mater. Interfaces*, 9 (2017) 5522.
[125] Z. Li, et al., *J. Mater. Chem. B*, 6 (2018) 6225.

[126] S. Sunny, et al., *P. Natl. A. Sci.*, 113 (2016) 11676.
[127] Q. Xie, et al., *ACS Appl. Mater. Interfaces*, 10 (2018) 11213.
[128] P.-Y. Qian, et al., *Nat. Rev. Microbiol.*, 20 (2022) 671.
[129] A. Eskhan, and D. Johnson, *Adv. Colloid Interfac.*, 310 (2022) 102796.
[130] Y. Feng, and Y. F. Cheng, *Chem. Eng. J.*, 315 (2017) 537.
[131] T. Du, et al., *Small*, 13 (2017) 1602020.
[132] Z. Deng, et al., *Addit. Manuf.*, 73 (2023) 103697.
[133] Y. Duan, et al., *Carbohyd. Polym.*, 304 (2023) 120504.
[134] S. Tian, et al., *Chem. Eng. J.*, 370 (2019) 1.
[135] L. Zhang, et al., *Appl. Catal. B*, 271 (2020) 118920.
[136] T. Yimyai, et al., *Adv. Funct. Mater.*, 31 (2021) 2102568.
[137] R. Deng, et al., *J. Mater. Chem. A*, 8 (2020) 7536.
[138] A. B. Tesler, et al., *Nat. Commun.*, 6 (2015) 8649.
[139] Y. B. Chong, et al., *Chem. Eng. J.*, 372 (2019) 496.
[140] A. Kaidarova, et al., *Nat. Biotechnol.*, 41 (2023) 1208.
[141] T. S. Moore, et al., *Annu. Rev. Mar. Sci.*, 1 (2009) 91.
[142] S. Zhang, et al., *Adv. Funct. Mater.*, 29 (2019) 1806434.
[143] S. Elmas, et al., *Environ. Sci. Technol.*, 55 (2021) 757.
[144] J. Zhang, et al., *Adv. Funct. Mater.*, 27 (2017) 1606544.
[145] A. V. Dudchenko, et al., *ACS Nano*, 9 (2015) 9930.
[146] H. Li, et al., *Adv. Funct. Mater.*, 33 (2023) 2212582.
[147] X. Yao, et al., *Adv. Funct. Mater.*, 30 (2020) 1909389.
[148] R. Dong, and B. Guo, *Nano Today*, 41 (2021) 101290.
[149] M. Alizadehgiashi, et al., *ACS Nano*, 15 (2021) 12375.
[150] Y. Liang, et al., *ACS Nano*, 15 (2021) 12687.
[151] Y.-Q. Zhao, et al., *ACS Nano*, 14 (2020) 2265.
[152] M. Garay-Sarmiento, et al., *Adv. Funct. Mater.*, 32 (2022) 2106656.
[153] F. Li, et al., *Chem. Eng. J.*, 467 (2023) 143546.
[154] P. Decristoforo, et al., *Clin. Microbiol. Infec.*, 24 (2018) 1101.e1.
[155] A. Hoxha, et al., 26 (2021) 1900646.
[156] J. Sabaté del Río, et al., *Nat. Nanotechnol.*, 14 (2019) 1143.
[157] P. Zhu, et al., *Small*, 17 (2021) 2170009.
[158] Y. Jin, et al., *P. Natl. A. Sci.*, 119 (2022) e2105459119.
[159] K. Manabe, et al., *ACS Nano*, 16 (2022) 16353.
[160] F. Wang, et al., *Sci. Adv.*, 8 (2023) eabp9369.
[161] H. Zhan, et al., *Adv. Funct. Mater.*, 33 (2023) 2211317.